NASA TECHNICAL NOTE

NASA TN D-4613

NASA TN D-4613

DETAILED PERFORMANCE OF A RADIAL-BLADED CENTRIFUGAL PUMP IMPELLER IN WATER

by Max J. Miller and Richard F. Soltis

Lewis Research Center
Cleveland, Ohio

DETAILED PERFORMANCE OF A RADIAL-BLADED CENTRIFUGAL

PUMP IMPELLER IN WATER

By Max J. Miller and Richard F. Soltis

Lewis Research Center
Cleveland, Ohio

NATIONAL AERONAUTICS AND SPACE ADMINISTRATION

ABSTRACT

Shrouded and unshrouded versions of a 7.44-in. - (18.89-cm-) diameter, radial-bladed centrifugal pump impeller were tested in room-temperature water. Detailed measurements permitted the calculations of both circumferential and spanwise distributions of flow and performance parameters over a wide range of flows. Primary emphasis is on essentially noncavitating flow conditions, although a limited amount of performance data obtained under cavitating flow conditions is presented.

STAR Category 12

DETAILED PERFORMANCE OF A RADIAL-BLADED CENTRIFUGAL PUMP IMPELLER IN WATER

by Max J. Miller and Richard F. Soltis

Lewis Research Center

SUMMARY

Shrouded and unshrouded versions of a 7.44-inch- (18.89-cm-) diameter, radial-bladed centrifugal pump impeller were tested in room-temperature water, and performance data were obtained under noncavitating and cavitating conditions. Detailed measurements permitted calculations of both circumferential and spanwise variations of flow and performance parameters over a wide range of flows. The results provide an improved understanding of flow conditions at design and off-design operation for this pump configuration. These results can also aid in interpreting analytical and empirical data for performance prediction.

Flow conditions were approximately constant around the impeller periphery but only over a narrow reference flow range that was somewhat below the design flow. At flows above and below the reference range, circumferential variations of flow conditions were measured. At higher than reference flows, pressure levels decreased with circumferential location; that is, the lowest pressure levels were obtained in the region of the volute tongue. At lower than reference flows, the circumferential gradient was reversed.

In the reference flow range, flow and performance parameters were nearly constant along the blade span for the shrouded impeller (representing a small tip-clearance - span ratio). For the unshrouded impeller (representing a high tip-clearance - span ratio), performance parameters generally decreased across the span toward the clearance space. At flows above the reference range, cavitation caused a decrease in performance in the tip-clearance region, while at flows below the reference range, secondary flows in the impeller produced a similar effect.

In general, the shrouded impeller gave higher levels of performance than those of the unshrouded impeller. This difference is attributed primarily to the relatively large tip-clearance - span ratio (13 percent) of the unshrouded configuration. However, as the net positive suction head H_{sv} was decreased, the cavitation that resulted caused a drop-off in head rise for the shrouded impeller at a slightly higher value of H_{sv} than that for the unshrouded impeller.

Real flow conditions, as measured, are compared with selected, assumed flow conditions and program inputs used in analytical procedures.

INTRODUCTION

Many of the advanced missions for space vehicle propulsion systems require pump operation over a range of flow rates. To the pump designer, these requirements are translated into the need for a wide, stable operating flow range and reasonably accurate methods for predicting performance over a range of operating conditions. The estimation of performance and flow conditions over the operating range of a centrifugal pump is generally based on measurements from similar pumps and/or computations from analytical procedures. Both of these methods usually require some interpretation on the part of the design analyst. The accuracy of the output from analytical procedures is dependent on the applicability of certain assumptions (e.g., steady, axisymmetric, and inviscid flow) and on the accuracy of certain inputs (e.g., deviation angle or slip factor). Empirical data are generally so limited that a clear understanding of flow conditions that result in a given performance characteristic is not obvious.

The purpose of this investigation was to provide detailed measurements of flow conditions near the inlet and outlet of a radial-bladed centrifugal pump. The data presented may be used to evaluate and improve the analytical procedures (such as that of ref. 1) used for pump design and the prediction of pump performance. Typical flow conditions that affect performance parameters over a range of operating conditions are examined. Data are presented for flow coefficients ranging from 22 to 173 percent of the design flow coefficient. For the pump investigated herein (outlet blade span of 0.191 in. or 0.485 cm), tip-clearance flows might be expected to exert a significant influence on the spanwise distribution of the measured parameters. To examine the magnitude of this influence, both shrouded and unshrouded versions of the impeller were tested in the cold-water tunnel at the Lewis Research Center. The data obtained from these tests show trends that might be expected when the tip clearance is varied from a relatively high ratio of tip clearance to outlet-blade span (13 percent for the unshrouded impeller) to a zero value (shrouded). When possible, the results are related to the visual studies of the unshrouded impeller flow reported in reference 2.

APPARATUS AND PROCEDURE

This section presents the nomenclature used to describe the impellers, a description of the flow passage geometry, and the locations of test instrumentation and measuring stations.

Nomenclature

The impeller nomenclature is presented in figure 1(b). The casing is the nonrotating part of the test section that encloses the impeller, the rotating outer cover of the impeller is the shroud, and the inner surface is called the hub. The distance from the hub to the tip of the blade (or to the inner surface of the shroud) is called the span. The edge of the span is called the blade tip, and the tip clearance is the gap between the blade tip and the stationary casing, or between the stationary casing and the shroud.

Flow and performance parameters at the five stations are also presented in figure 1(b). Station 1 is the inlet measuring station; station 2 extends along the blade leading edge. Flow conditions at this station are calculated from measured values at station 1. Station 3 is a calculation station at the blade trailing edge. Station 4 is the impeller outlet measuring station in the radial vaneless-diffuser section. At station 4,

Survey measurement locations

Percent of span from hub	Inlet		Outlet	
	Distance from casing, e		Distance from casing, f	
	in.	cm	in.	cm
90	0.11	0.25	-----	-----
~70	.31	.79	0.075	0.191
50	.56	1.42	.125	.317
~30	.76	1.93	.175	.444
15	.96	2.44	----	----

(a) Front view.

(b) Side view.
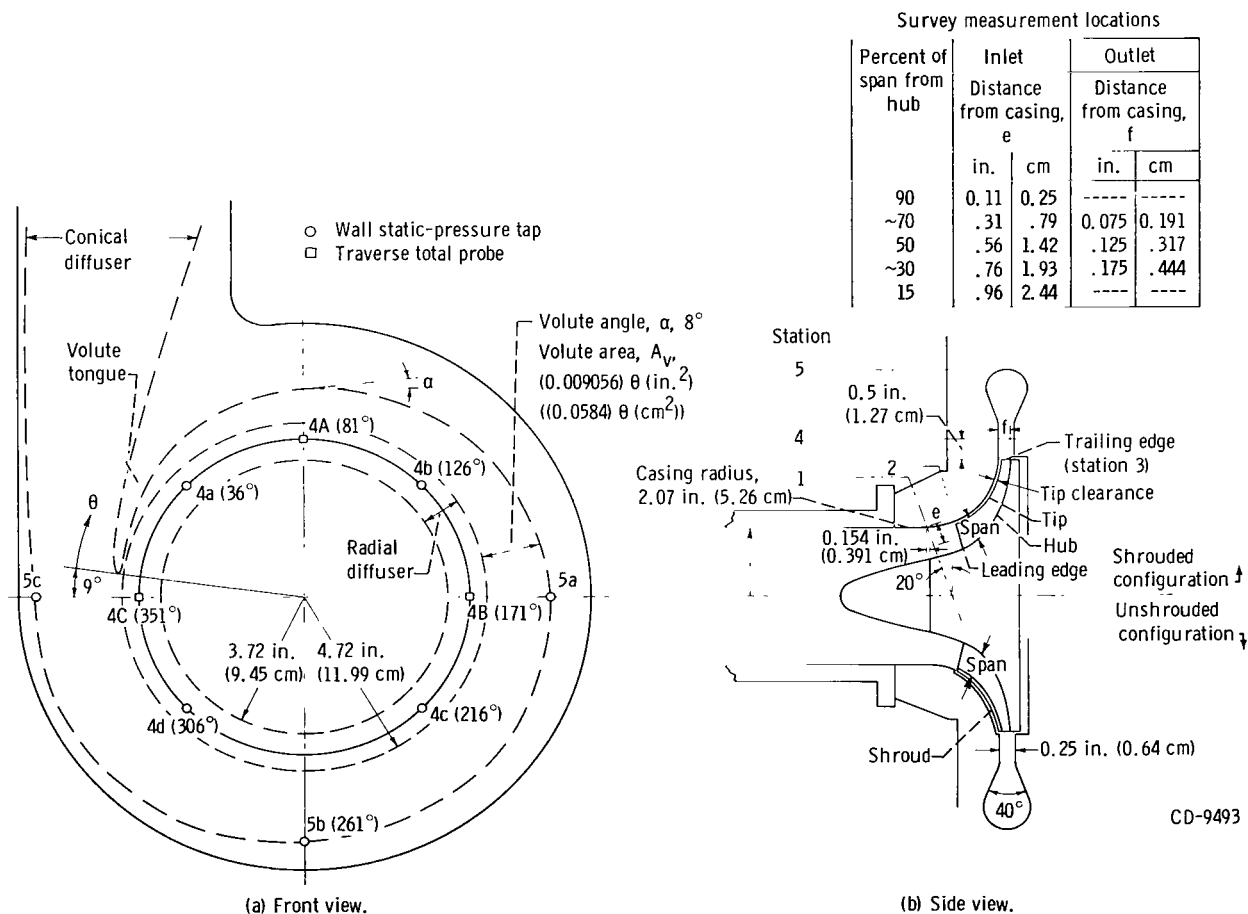
Figure 1. – Nomenclature of pump and instrumentation locations.

3

seven circumferential measurement locations are identified by letters (fig. 1(a)). Station 5 is the measuring station at the periphery of the volute section. At this station, three circumferential locations are also identified by letters (fig. 1(a)). The table in figure 1(b) gives the inlet and the outlet survey measurement locations in the meridional plane. Throughout this report, these station numbers and location letters are used as subscripts to indicate the station and location for which a parameter applies. All symbols are defined in appendix A.

Pump Description

A research radial-bladed centrifugal impeller and a single-discharge volute casing were used for this investigation. Both a shrouded and an unshrouded impeller were

Figure 2. - Unshrouded and shrouded test impellers.

tested. The shrouded impeller was fabricated by furnace brazing a shroud to the blade tips of an unshrouded impeller. A photograph of the two impellers is presented in figure 2.

The impeller was designed by a procedure similar to the one presented in reference 1. In the design of the impeller, splitter blades were judiciously located so that calculated reverse flow, or eddy, regions were eliminated at the design flow coefficient.

4

TABLE I. - IMPELLER GEOMETRY AND COORDINATES

[Blade shape, $\gamma = \dfrac{0.92(z - 2)^2}{r}$, where γ is angle from

radius through suction surface at outlet tip of main

blade, z is axial dimension, and r is inlet radius.]

Large splitter blade
Small splitter blade
Main blade

Radius, 0.19 in.
(0.48 cm)

Radius, 4.75 in.
(12.05 cm)

CD-9492
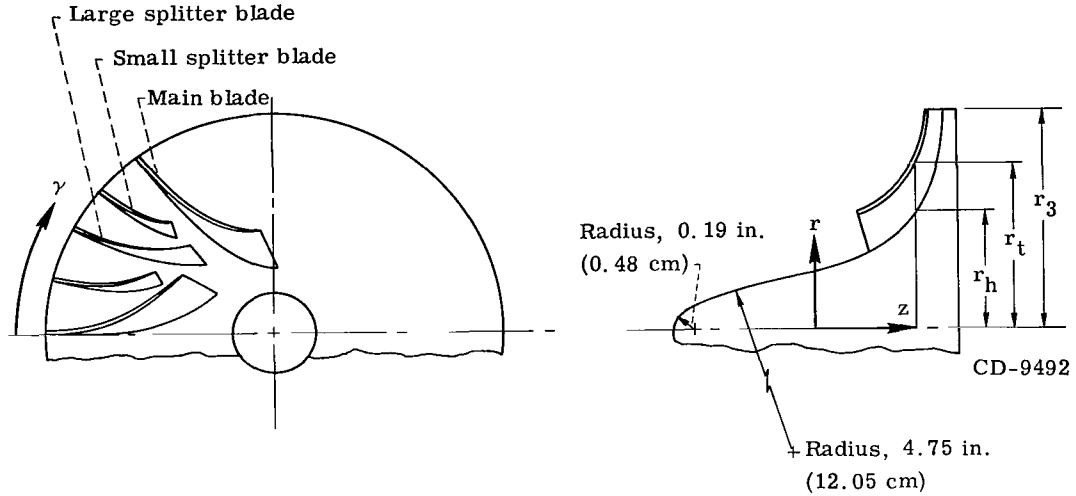
Axial dimension, z		Hub radius, r_h		Tip radius, r_t	
in.	cm	in.	cm	in.	cm
0.000	0.000	0.791	2.009	------	-----
.200	.508	.861	2.187	------	-----
.400	1.016	.942	2.393	------	-----
.600	1.524	1.050	2.667	------	-----
.800	2.032	1.192	3.028	------	-----
.900	2.286	1.278	3.246	[a]2.112	5.364
1.000	2.540	[a]1.378	3.500	2.164	5.497
1.150	2.921	------	-----	[b]2.270	5.766
1.200	3.048	1.606	4.079	2.310	5.867
1.320	3.353	[b]1.760	4.470	------	-----
1.380	3.505	------	-----	[c]2.485	6.312
1.400	3.556	1.880	4.775	2.510	6.375
1.530	3.886	[c]2.035	5.169	------	-----
1.600	4.064	2.216	5.629	2.806	7.127
1.800	4.572	2.610	6.629	3.600	9.144
1.809	4.595	------	-----	3.718	9.444
2.000	5.080	3.718	9.444	------	-----

[a]Main blade leading edge.
[b]Large splitter blade leading edge.
[c]Small splitter blade leading edge.

5

Some of the pertinent design parameters for the impeller are as follows:

Flow coefficient, $\overline{\varphi}_D$ 0.363

Head-rise coefficient, $\overline{\psi}_D$ 0.72

Hydraulic efficiency, $\overline{\eta}$, percent 80

Slip factor, μ 0.9

Incidence angle, i, deg 2

Inlet radius ratio, $r_{h,2}/r_{t,2}$ 0.65

Inlet tip radius, $r_{t,2}$, in. (cm) 2.112 (5.35)

Discharge radius, r_3, in. (cm) 3.718 (9.44)

Along with the coordinates presented in table I, the blade shape is defined by the equation

$$\gamma = \frac{0.92(z - 2)^2}{r}$$

where γ is the angle from the radius through the suction surface at the outlet tip of the main blade, z is the axial dimension, and r is the inlet radius. The coordinates defining the locations of the leading edge, trailing edge, hub, and tip of the blades are also given in table I. The impeller has seven main blades, seven large splitter blades, and fourteen small splitter blades. The blades have a constant thickness of 0.062 inch (1.575 mm) perpendicular to the mean camber line.

The impeller discharge flow passes through a straight radial vaneless-diffuser section, is collected in a volute, and is diffused through a single conical diffuser before reaching the outlet pipe. A sketch of the discharge casing is shown in figure 1(a). In general, the method given by reference 3 was used to design the volute for a specific speed N_s of 1154, an average flow coefficient $\overline{\varphi}$ of 0.363, and an average head-rise coefficient $\overline{\psi}$ of 0.72. However, the width and the radial extent of the radial vaneless diffuser were selected to allow adequate room for instrumentation. Additional volute design information is given in figure 1(a).

Test Facility

This investigation was conducted in the Lewis cold water tunnel, which is a closed-loop pump test facility. A diagram and a photograph of the tunnel are shown in figures 3 and 4, respectively. A more detailed description of the facility is given in reference 4. The tunnel was filled with water that had been passed through a filter capable of removing particles larger than 5 microns in diameter. The air content of the water was reduced to less than 1 ppm by weight and was maintained below 3 ppm during the testing.

Heat exchanger

Venturi meter

Degasifying
tank

Vacuum
pump

Control valve

Filter

Straightening tubes

Orifice meter

Flow

Pressure-controlling
accumulator

Test section

CD-9621

Gearbox

3000-hp
$(2.23 \times 10^6$-W)
variable-frequency
alternating-current
motor
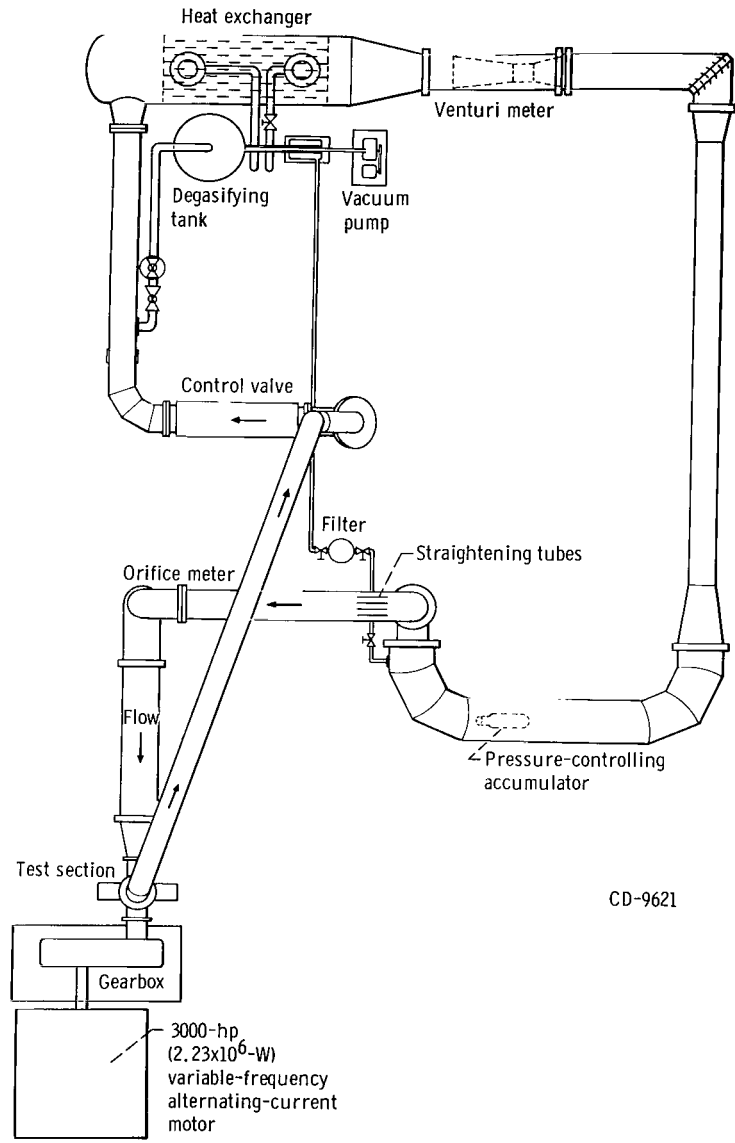
Figure 3. - Diagram of test facility.
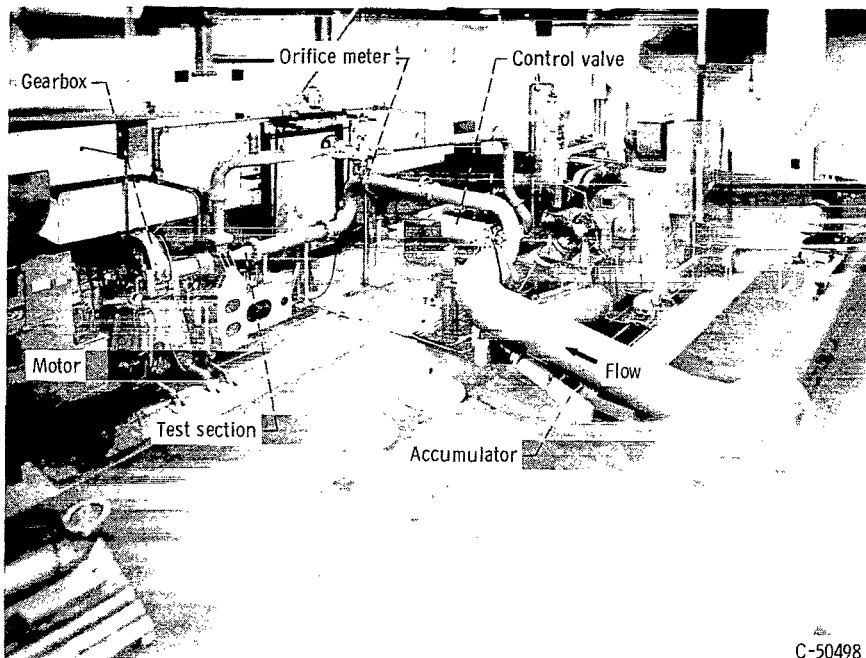
Figure 4. - Test facility.

Test Procedure and Instrumentation

Performance was measured with the speed N and net positive suction head H_{sv} maintained constant while the flow rate Q was varied. The performance, measured at a net positive suction head H_{sv} of 192 feet per pound force per pound mass (58.5 m-N/kg), is referred to as noncavitating, although some effects of cavitation on performance were noted at $\overline{\varphi} > 0.5$. A higher H_{sv} could not be used because of instrumentation limitations. Visual observations of the unshrouded impeller (ref. 2) confirmed that cavitation was occurring in the segment of the impeller near the volute tongue (fig. 1(a)) at $\overline{\varphi} > 0.5$.

At each selected flow rate, measurements were taken at the inlet measuring station (station 1), the outlet measuring station (station 4), and the volute measuring station (station 5). At station 1 (fig. 1(b)), survey measurements of total pressure, static pressure, and flow angle were made at five span positions given in the table of figure 1(b). Because the flow at station 1 was assumed to be axisymmetric, measurements were taken with a wedge static-pressure probe at one circumferential location and with a total-pressure probe at another. The centerlines of these probes were inclined 20° from the radial direction to keep them approximately perpendicular to the meridional streamlines over most of the passage.

At the outlet measuring station (station 4), surveys of total pressure and flow angle were made at three circumferential locations: 4A, 4B, and 4C (fig. 1(a)). These measurements were made at three span positions that are given in the table of figure 1(b). No static-pressure probes were used at station 4; instead, static pressure was measured with wall static taps at locations 4a, 4b, 4c, and 4d (fig. 1(a)).

At the volute measuring station (station 5), wall static taps were located at 5a, 5b, and 5c (fig. 1(a)).

(a) Outlet total-pressure and flow-angle claw.

(b) Static-pressure wedge.

(c) Inlet total-pressure and flow-angle cobra.
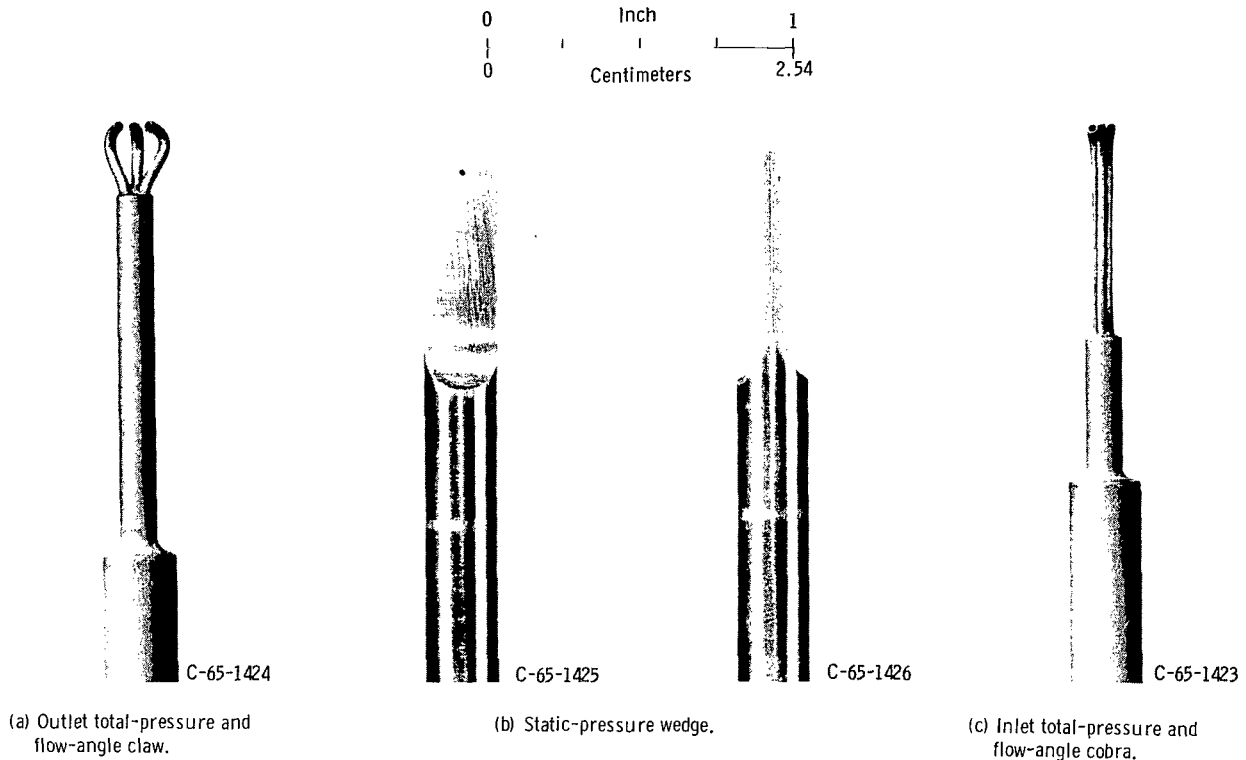
Figure 5. - Probes.

Figure 5 is a photograph of the survey probes, all of which were automatically alined with the flow by means of a null-balance system. The wedge static-pressure probe was calibrated in a low-speed air tunnel. Flow rate, rotational speed, and water temperature were measured with an orifice flowmeter, a magnetic speed pickup and electronic tachometer, and a thermocouple, respectively. The length of straight pipe downstream of the orifice was too short to use a standard discharge coefficient, so the orifice was calibrated in position with a venturi meter, which is also in the loop. The venturi was not used during testing because the venturi pressure drop was too small to measure accurately with the strain-gage transducers used in conjunction with the recording equipment.

The orifice was calibrated at a flow rate higher than the test flow rates by using a manometer to measure the venturi pressure drop.

The estimated inherent accuracies of the measuring and recording systems were as follows:

Flow rate, Q_o, percent of design flow . . . . ±1.0

Rotor head rise, ΔH, percent at design flow. . . . . ±1.0

Velocity head, $V^2/2g_c$, percent at design flow . . . . ±3.0

Outlet flow angle, β_4, deg . . . . ±1.0

Rotative speed, N, percent . . . . ±0.5

Inlet flow angle, β_1, deg . . . . ±5.0
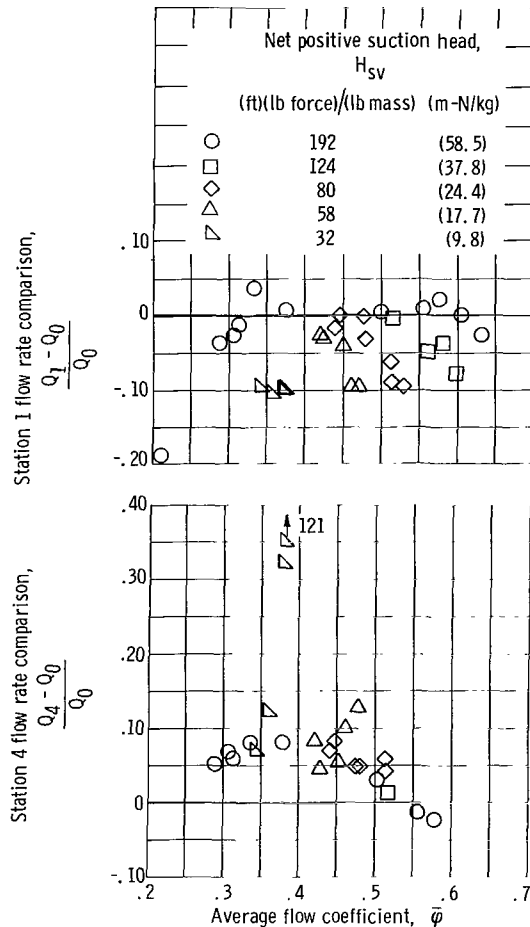
(a) Shrouded impeller.

Figure 6. - Comparison of integrated flow rate at impeller inlet and outlet measuring stations with those measured by orifice meter.
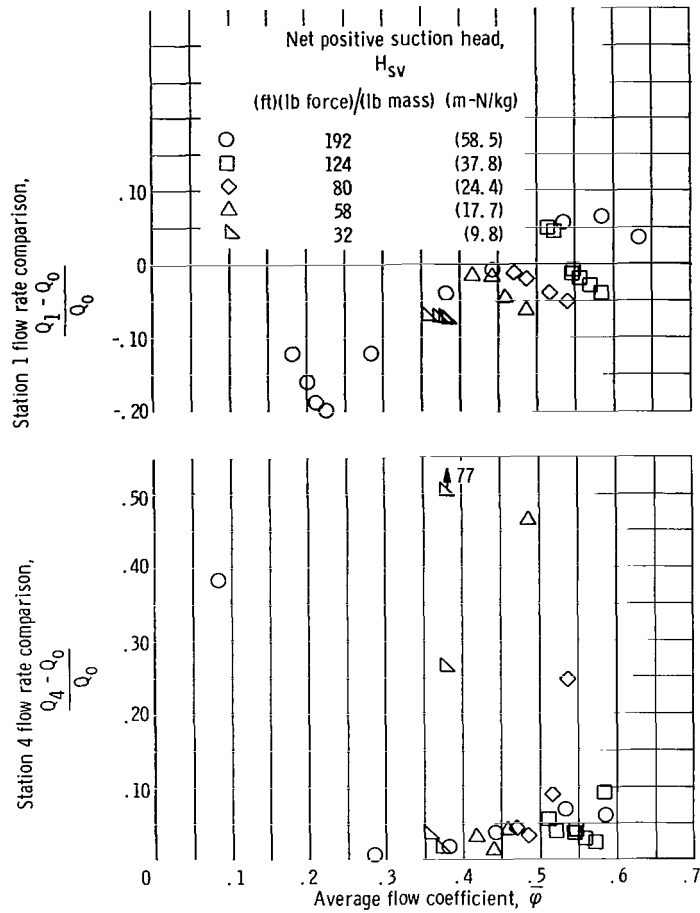
(b) Unshrouded impeller.

Figure 6. - Concluded.

A check on the reliability of the survey measurements is obtained from the integrated flow rate comparisons shown in figure 6. The difference between the flow rate calculated from survey measurements at stations 1 and 4 and the flow rate measured with the orifice is shown as a percentage of the orifice flow rate. In calculating the integrated flow rate, no boundary layer blockage was used. If a small boundary layer is assumed, a good comparison would be approximately 2 to 5 percent rather than 0 percent. At station 1 (fig. 6), most of the comparisons fall in the range of 0 to -10 percent. These comparisons are not considered good. The comparisons for the noncavitating H_{sv} (192 ft-lb force/lb mass or 58.5 m-N/kg) are, however, better than those for the lower H_{sv}, which suggests that at a lower H_{sv} probe cavitation may be affecting the measurements, especially the static-pressure measurements. At $\bar{\varphi} < 0.2$ large negative values of the comparisons reflected a flow reversal at the inlet, but the values are not shown. At sta-

11

tion 4 (fig. 6), most of the comparisons fall in the range from 0 to 10 percent. These comparisons are considered reasonably good for the outlet of a centrifugal machine.

Computation Procedure

All measurements were taken at an impeller rotational speed of 3000 rpm ($U_{t,3}$ = 97.34 ft/sec or 29.67 m/sec); however, where possible, the data are presented in the form of coefficients to eliminate speed as a variable. The following pump performance and velocity-diagram parameters were calculated:

(1) Head-rise coefficient, ψ

(2) Flow coefficient, φ

(3) Hydraulic efficiency, η

(4) Net positive suction head, H_{sv}

(5) Flow angle, β

(6) Incidence angle, i

(7) Deviation angle, δ

(8) Slip factor, μ

The calculation of these parameters was complex because of the geometry of the pump. For instance, at the inlet, the curved walls of the passage made definition of streamline locations, streamline curvatures, and flow areas somewhat difficult. At the outlet, the volute casing imposed a circumferential gradient of flow conditions at most flow coefficients, which made determination of the average flow condition difficult. Therefore, simplifying assumptions were made to expedite the calculation of the performance and the velocity-diagram parameters. The assumptions and procedures used are outlined in the remainder of this section. The flow parameter equations are given in appendix B.

An average axial velocity at the blade leading edge, based on the orifice flow rate and the annulus area, and the inlet blade tip speed were used to calculate the average inlet flow coefficient $\overline{\varphi}$ (eq. (B15)). However, local flow coefficients φ were calculated from the local meridional velocity (based on measurements of total pressure, static pressure, and flow angle) and from the inlet blade tip speed (eq. (B1)).

Local flow coefficients and incidence angles were calculated at the blade leading edge (station 2, fig. 1(b)) with the use of total-pressure measurements taken at the inlet measuring station (station 1) and by the procedure outlined in appendix C. Briefly, the procedure assumed no total-pressure loss from station 1 to station 2 and required that continuity and radial equilibrium (including the curvature term) be satisfied at the blade leading edge.

Outlet total pressure was measured at three span positions at three circumferential locations 4A, 4B, and 4C. Local head-rise coefficients were calculated for these nine locations. This calculation was possible since the inlet total head was approximately constant along the span, and local head-rise coefficients could be computed without defining streamline flow. Also, an average head-rise coefficient $\overline{\psi}$ was calculated from the arithmetic average of the nine local ψ-values.

Velocity-diagram components were calculated for the three span positions at station 4 by the use of arithmetic average values of total pressure, wall static pressure, and flow angle. The total pressure and flow angles used were arithmetic averages of the measurements taken at circumferential locations 4A, 4B, and 4C. A constant static pressure across the span equal to the arithmetic average of the wall static pressures measured at circumferential locations 4a, 4b, 4c, and 4d was used. These outlet velocity diagrams are most valid near $\overline{\varphi} = 0.3$, where data showed that the pump was operating approximately axisymmetrically. Velocity-diagram parameters were calculated from the components of these velocity diagrams.

Velocity-diagram components and parameters were also calculated at the blade trailing edge (station 3) with the velocity diagrams for the outlet measuring station (station 4) and the procedure outlined in appendix C. The procedure consisted of applying conservation of angular momentum and the condition of continuity at the two stations.

An average hydraulic efficiency (eq. (B20)) was calculated with the use of an average $\overline{\psi}_{id}$ (eq. (B19)) and the measured $\overline{\psi}$.

RESULTS AND DISCUSSION

The data presented primarily describe the performance and flow conditions across the impeller. Results from both the shrouded and the unshrouded version of the impeller are presented.

Overall Noncavitating Performance

The overall performance of the two impellers is shown in figure 7. The arithmetic-averaged head-rise coefficient $\overline{\psi}$ and the hydraulic efficiency $\overline{\eta}$ are shown as a function of the average flow coefficient $\overline{\varphi}$. The maximum φ for which ψ is shown was set by instrumentation limitations, rather than by the loop pressure-loss characteristic. The minimum φ for which a ψ is shown was set arbitrarily, although it was possible to operate the pump from 173 percent of $\overline{\varphi}_D$ down to shutoff with no unusual rig vibrations or noise. The calculation of $\overline{\eta}$ for $\overline{\varphi} < 0.285$ was impossible because of instrumenta-
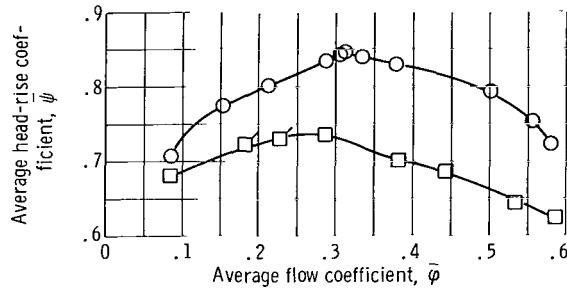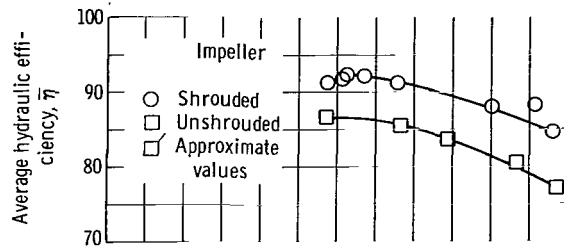
Figure 7. - Overall performance for noncavitating conditions. Impeller outlet tip speed, 97.34 feet per second (29.67 m/sec); net positive suction head, 192 feet per pound force per pound mass (58.5 (m-N/kg).

tion limitations in measuring the outlet wall static pressure needed to calculate the ideal head-rise coefficient.

Both $\overline{\psi}$ and $\overline{\eta}$ of the shrouded impeller exceeded those of the unshrouded impeller. The $\overline{\psi}$ of the unshrouded impeller was closest to the $\overline{\psi}$ of the shrouded impeller at a low $\overline{\varphi}$. The lower $\overline{\psi}$ of the unshrouded impeller resulted from a lower energy addition and higher losses. For example, at $\overline{\varphi} = 0.363$ and where $\overline{\eta} = (\overline{\psi}/\overline{\psi}_{id})100 = (\overline{\psi}_{id} - \overline{\psi}_{L})/\overline{\psi}_{id}100$, the following table compares the coefficients of the energy addition $\overline{\psi}_{id}$ and loss $\overline{\psi}_{L}$ for the two impellers:

Impeller	Energy addition, $\overline{\psi}_{id}$	Energy loss, $\overline{\psi}_{L}$
Shrouded	0.91	0.077
Unshrouded	.823	.117

14

Values of $\overline{\psi}$ and $\overline{\eta}$ from figure 7 were used in the calculation of $\overline{\psi}_{id}$ and $\overline{\psi}_L$. Note that for a radial-bladed impeller $\overline{\psi}_{id} = \overline{\mu}$. The preceding calculations are based on the hydraulic efficiency $\overline{\eta}$, and for this reason $\overline{\psi}_L$ does not include leakage losses for the shrouded impeller.

The two sets of results represent the trends that would be expected from an unshrouded centrifugal pump impeller as tip clearance is varied from a relatively high ratio of tip clearance to outlet-blade span (13 percent) to a zero (shrouded) value.
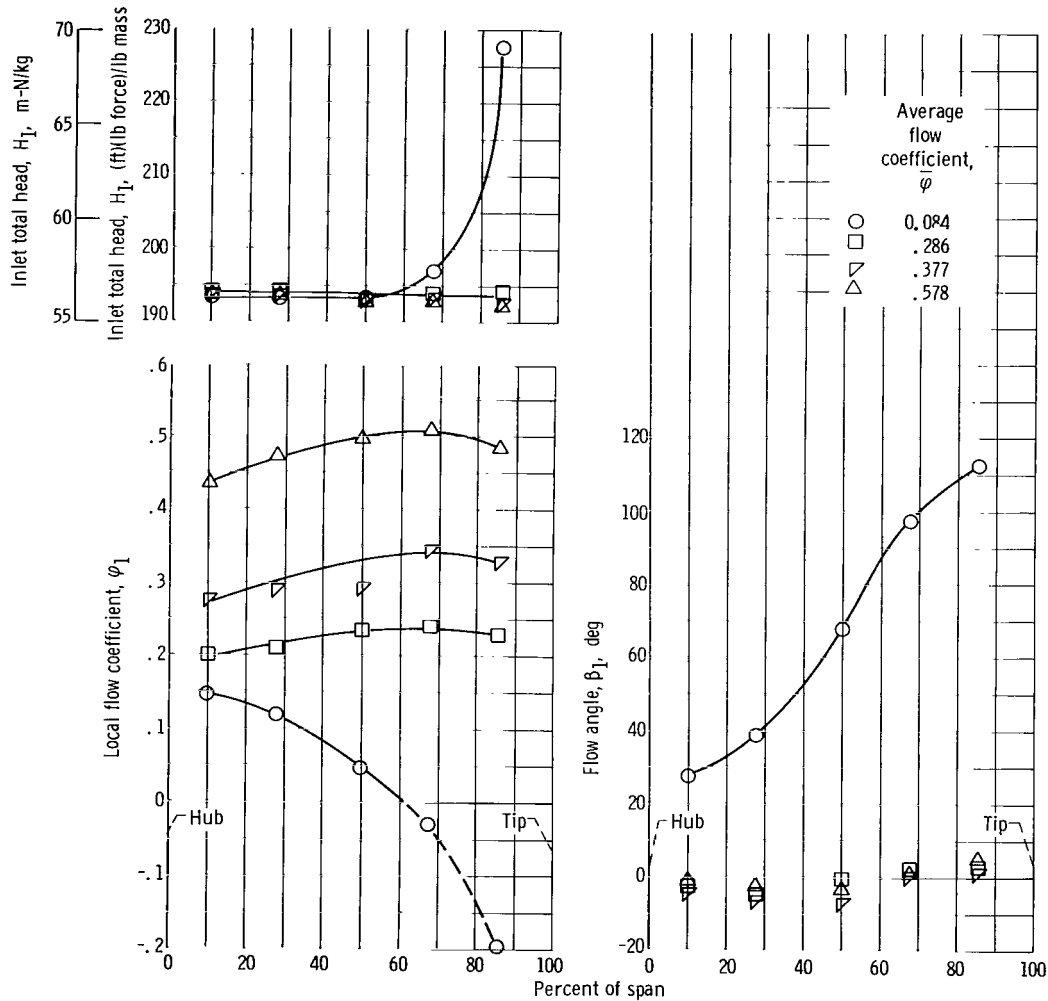
(a) Shrouded impeller.

Figure 8. - Spanwise distributions of measurements taken at inlet measuring station 1. Net positive suction head, 192 feet per pound force per pound mass (58.5 m-N/kg).
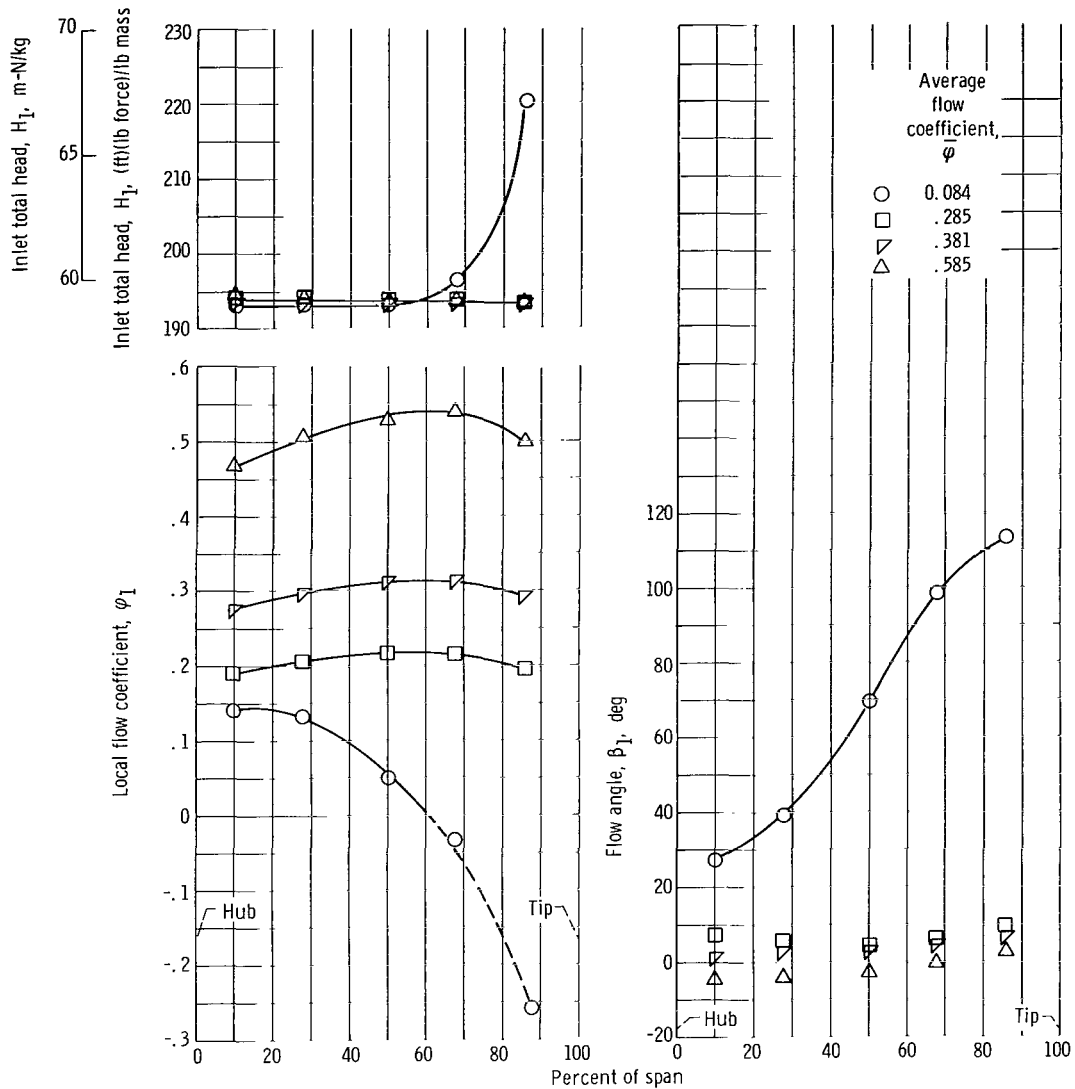
(b) Unshrouded impeller.

Figure 8. – Concluded.

Detailed Noncavitating Performance

Inlet parameters. - In figure 8, the flow conditions at the inlet measuring station (station 1) are shown as a function of the percentage of span. The exact measurement locations are given in the table of figure 1(b). The results for the shrouded impeller (fig. 8(a)) and the unshrouded impeller (fig. 8(b)) show little or no differences; therefore, the following discussion of inlet flow conditions applies equally well to either impeller.

The curves for $\bar{\varphi} = 0.377$ in figure 8 show that the total head H_1 is essentially constant along the span, but that the local flow coefficient φ increases slightly toward
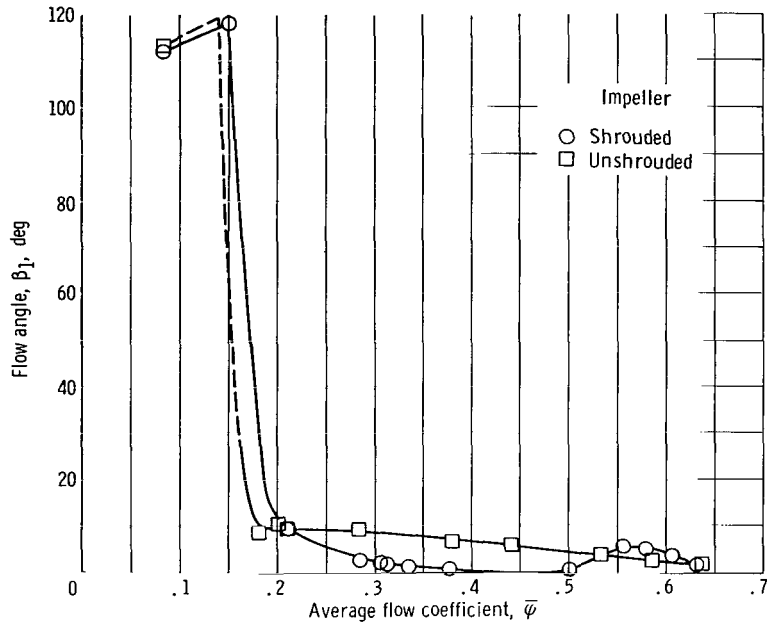
Figure 9. - Flow angle measured at 85 percent of span from hub at inlet measuring station 1. Net positive suction head, 192 feet per pound force per pound mass (58.5 m-N/kg).

the tip because of the passage curvature. At $\bar{\varphi} > 0.377$ the trends are the same, but the magnitudes reflect the change in $\bar{\varphi}$. With one exception, the flow angle β_1 was within $\pm 7^O$ of 0 or the axial direction for $\bar{\varphi} \geq 0.377$. Because of the low velocity head at the inlet measuring station and the limitations of the null-balancing system, the inherent accuracy of the equipment measuring the inlet flow angles is approximately $\pm 5^O$. For this reason, the flow angles measured at $\bar{\varphi} = 0.377$ are not considered indicative of prerotation but probably indicate the design condition of $\beta_1 = 0$.

At $\bar{\varphi} = 0.084$, a reverse flow is indicated by the increase in H_1, and $\beta_1 > 90^O$ at 85 percent of the span (fig. 8). The $\beta_1 > 90^O$ resulted in the calculation of a negative φ in the passage from approximately 60 to 100 percent of the span. The increase in H_1 (fig. 8) indicates a reverse flow carrying energized fluid out of the blade passage and into the inlet pipe near the outer wall. The approximate $\bar{\varphi}$ at which the reverse flow became apparent at station 1 (fig. 1(b)) is indicated in figure 9. The β_1 at 85 percent of the span is shown as a function of $\bar{\varphi}$ for both impellers. At a $\bar{\varphi}$ slightly below 0.2, β_1 increased abruptly to values greater than 90°.

The distributions of local flow coefficients and incidence angles calculated along the span at the blade leading edge (station 2) are shown in figure 10. At all flows shown for both impellers, the i and φ_2 increase slightly toward the blade tip because of the passage curvature. Values are not shown for $\bar{\varphi} = 0.084$ because the calculations outlined in appendix C were not valid for a reverse flow. This procedure to calculate φ_2 was

17
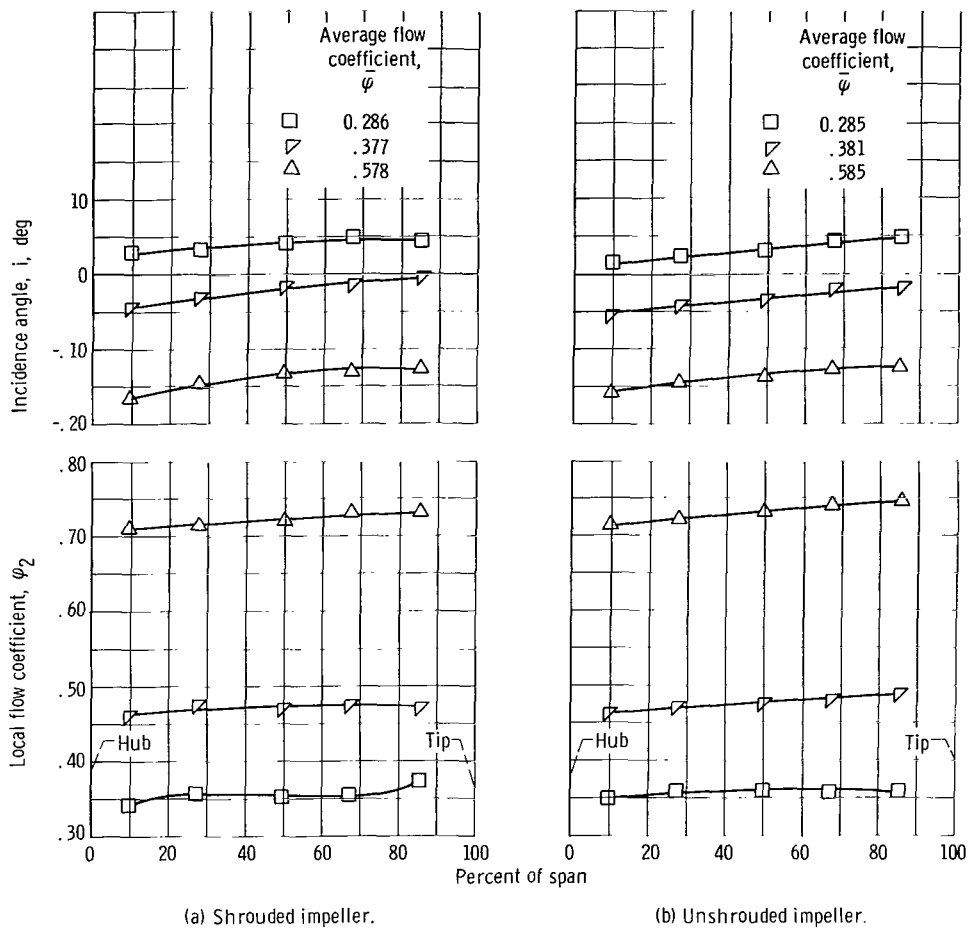
Figure 10. - Spanwise distributions of calculated parameters at blade leading edge (station 2). Net positive suction head, 192 feet per pound force per pound mass (58.5 m-N/kg).

necessary because the area change from station 1 to station 2 was large enough to cause errors of 10^0 or more in i if φ_1 were used to calculate β_2'.

The inlet flow conditions at all but a low $\overline{\varphi}$ probably could be calculated from passage considerations (including streamline curvature and boundary-layer effects). However, at a low $\overline{\varphi}$ a reverse flow from the impeller into the inlet precludes such calculations.

Outlet measurements. - In this section, measurements taken at two stations (4 and 5) downstream of the impeller are presented. At station 4 (the outlet measuring station), measurements of total pressure and flow angle, from survey probes, and static pressure, from wall static taps, define impeller performance. Pressure gradients around the volute are obtained from wall static-pressure measurements taken at the volute periphery (station 5). Significant flow conditions and performance trends indicated by the measurements are discussed briefly.
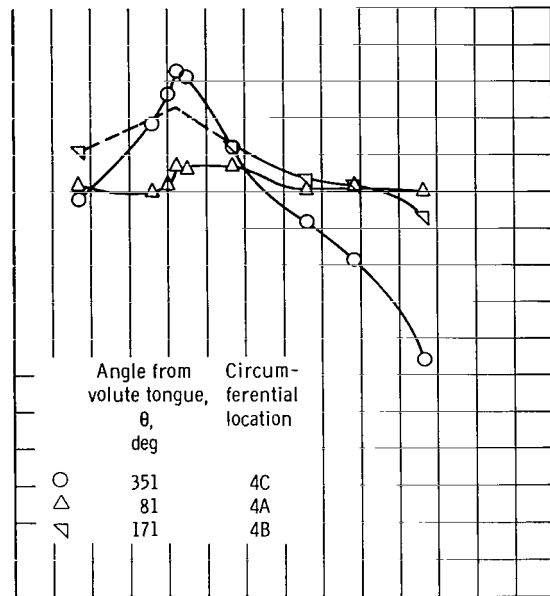
18

Local head-rise coefficient, ψ

(a) Shrouded impeller at 70 percent of span from hub.

(b) Unshrouded impeller at 70 percent of span from hub.

	Angle from volute tongue, θ, deg	Circumferential location
○	351	4C
△	81	4A
▽	171	4B
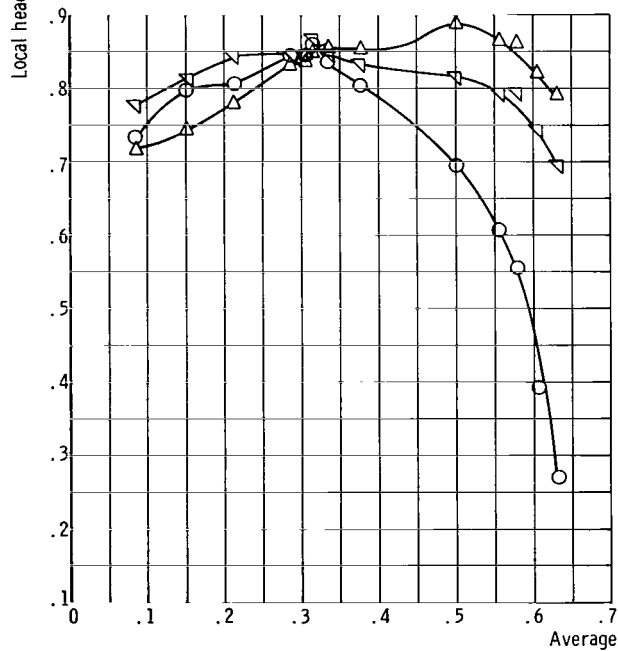
(c) Shrouded impeller at 50 percent of span from hub.

(d) Unshrouded impeller at 50 percent of span from hub.

Average flow coefficient, $\bar{\varphi}$
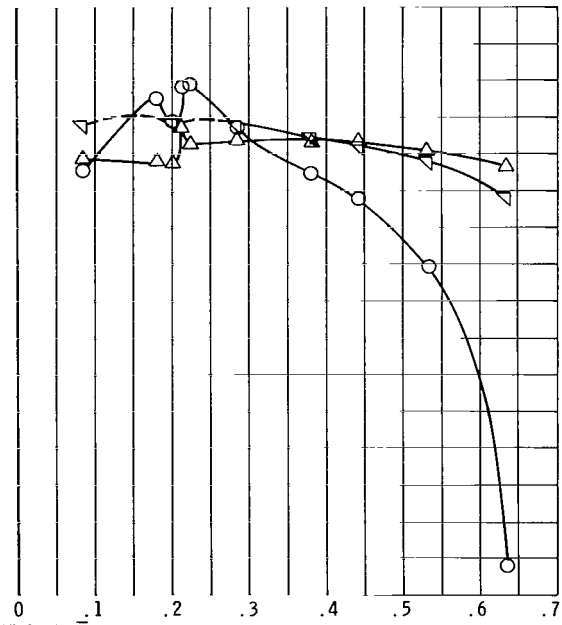
Figure 11. - Local head-rise coefficients of station 4. Net positive suction head, 192 feet per pound force per pound mass (58.5 m-N/kg).
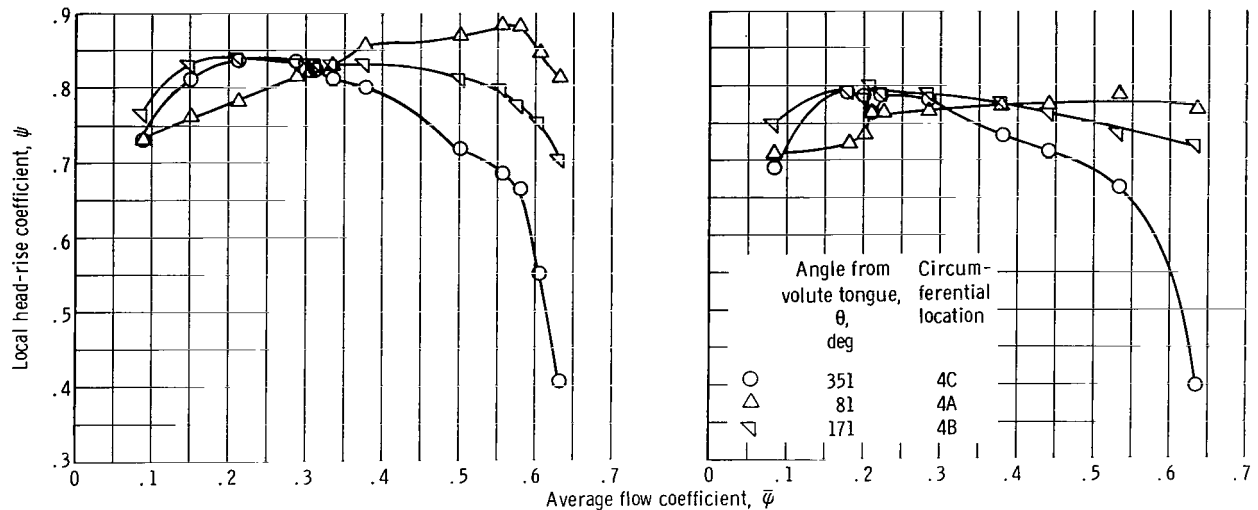
(e) Shrouded impeller at 30 percent of span from hub.   (f) Unshrouded impeller at 30 percent of span from hub.

Figure 11. – Concluded.

At station 4, the local head-rise coefficients ψ_4 and the flow angles β_4 for three circumferential locations (4A, 4B, and 4C, located as shown in fig. 1(a)) are presented in figures 11 and 12, where they are shown as a function of $\overline{\varphi}$ for three span positions. The wall static head at four circumferential locations (4a, 4b, 4c, and 4d as shown in fig. 1(a)) is presented in figure 13 as a function of $\overline{\varphi}$. In figure 14, the wall static head h_5 around the volute periphery is presented as a function of $\overline{\varphi}$. These curves can be used to show parametric variations over the flow range, to show circumferential variations at a given $\overline{\varphi}$, and to compare results from the two impellers. Some of the points on these curves are missing because of transducer limitations (thus, the curve is represented by a dashed line).

Circumferential distributions of outlet parameters. - The measurements for both impellers (figs. 11 to 14) indicate that only in a relatively narrow range of $\overline{\varphi}$ are the flow conditions the same, or nearly the same, at all points around the impeller. This reference range centers about a $\overline{\varphi} \simeq 0.32$.

As $\overline{\varphi}$ was increased from the reference range, significant circumferential gradients were noted in all the measurements. Measurements of ψ_4 (fig. 11), β_4 (fig. 12), and h_4 (fig. 13) decrease with circumferential position. Minimum values were measured near the volute tongue ($\theta = 360^{\circ}$). Static-pressure measurements h_5 (fig. 14) around the volute periphery show that an outlet static-pressure gradient was imposed on the impeller. This back pressure also decreased with circumferential position. The impeller was forced to operate with a circumferential variation of back pressure that resulted in circumferential gradients of impeller performance. At $\overline{\varphi}$ above the reference $\overline{\varphi}$ range, circumferential trends of measurements were identical for the two impellers, but the

20
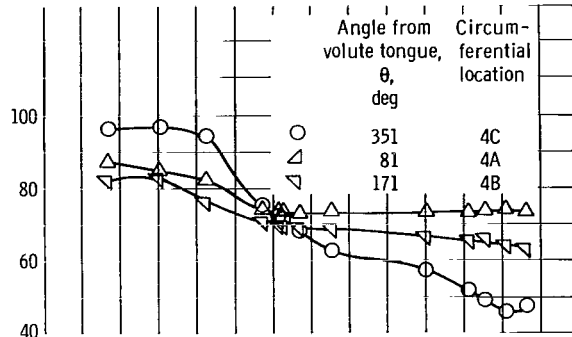
(a) Shrouded impeller at 70 percent of span from hub.
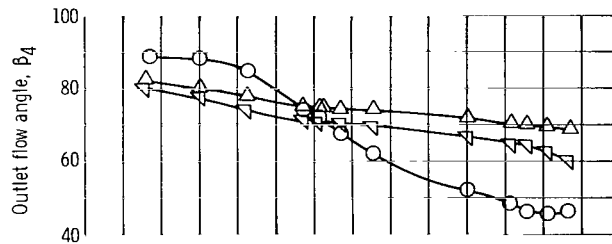
(b) Shrouded impeller at 50 percent of span from hub.
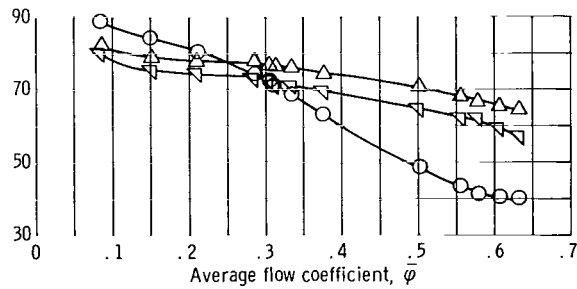
(c) Shrouded impeller at 30 percent of span from hub.

Figure 12. – Local outlet flow angles at station 4. Net positive suction head, 192 feet per pound force per pound mass (58.5 m-N/kg).
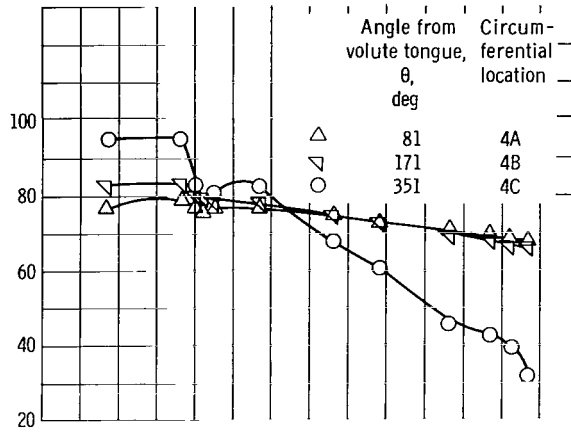
(d) Unshrouded impeller at 70 percent of span from hub.
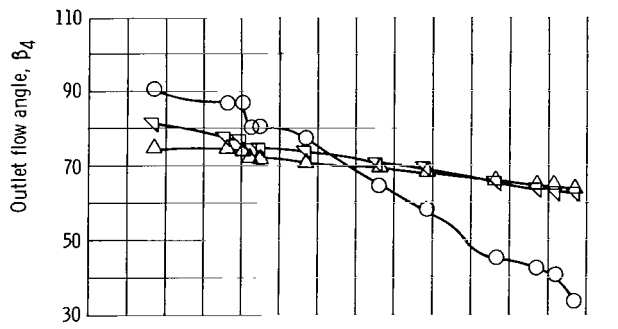
(e) Unshrouded impeller at 50 percent of span from hub.
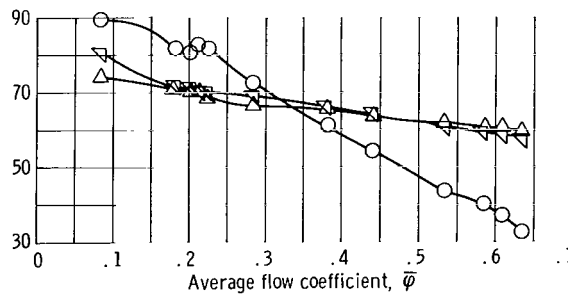
(f) Unshrouded impeller at 30 percent of span from hub.

Figure 12. - Concluded.

Outlet wall static head, h_4, m-N/kg

Outlet wall static head, h_4, (ft\\lb force)/lb mass

	Angle from volute tongue, θ, deg	Circumferential location
○	126	4b
◇	216	4c
▽	306	4d
◁	36	4a

(a) Shrouded impeller.

(b) Unshrouded impeller.

Average flow coefficient, $\bar{\varphi}$
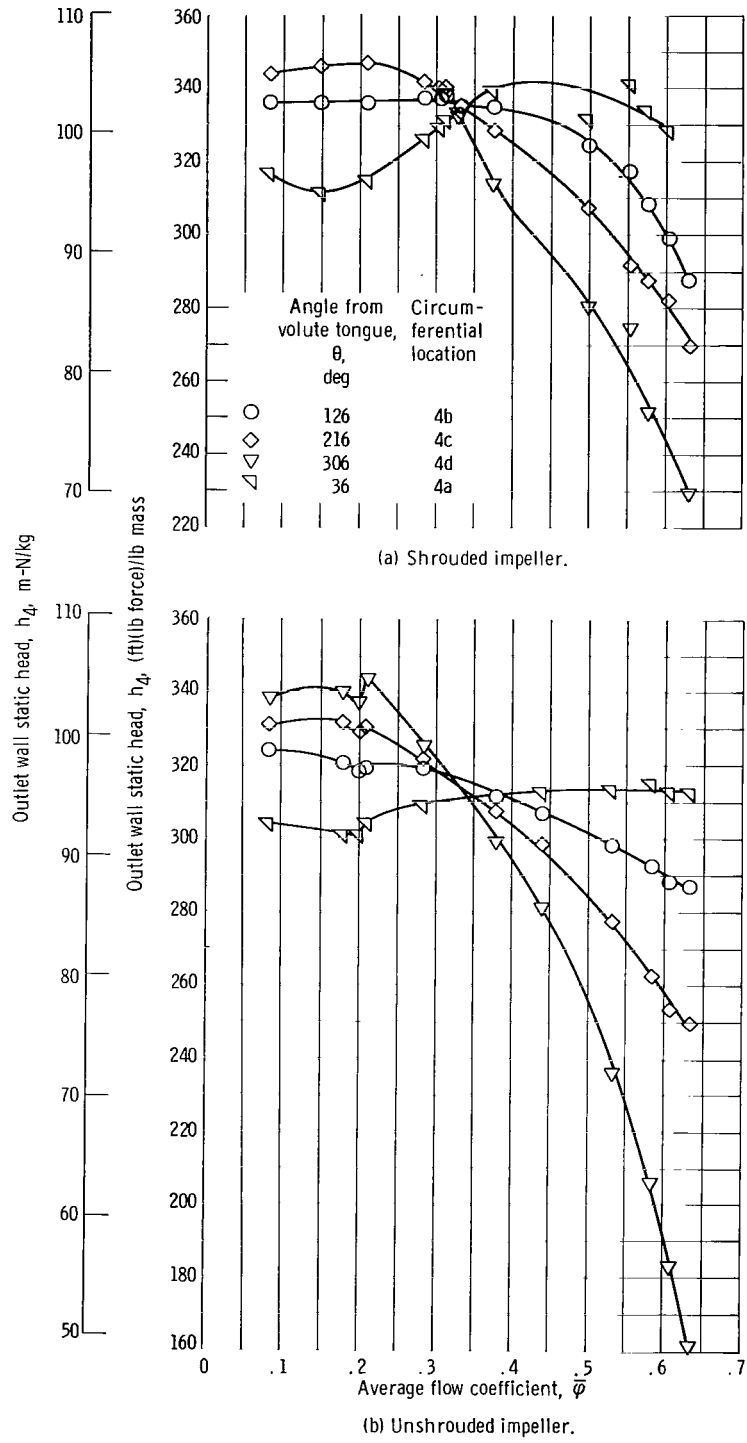
Figure 13. – Wall static head at four circumferential locations at outlet measuring station 4. Net positive suction head, 192 feet per pound force per pound mass (58.5 m-N/kg).
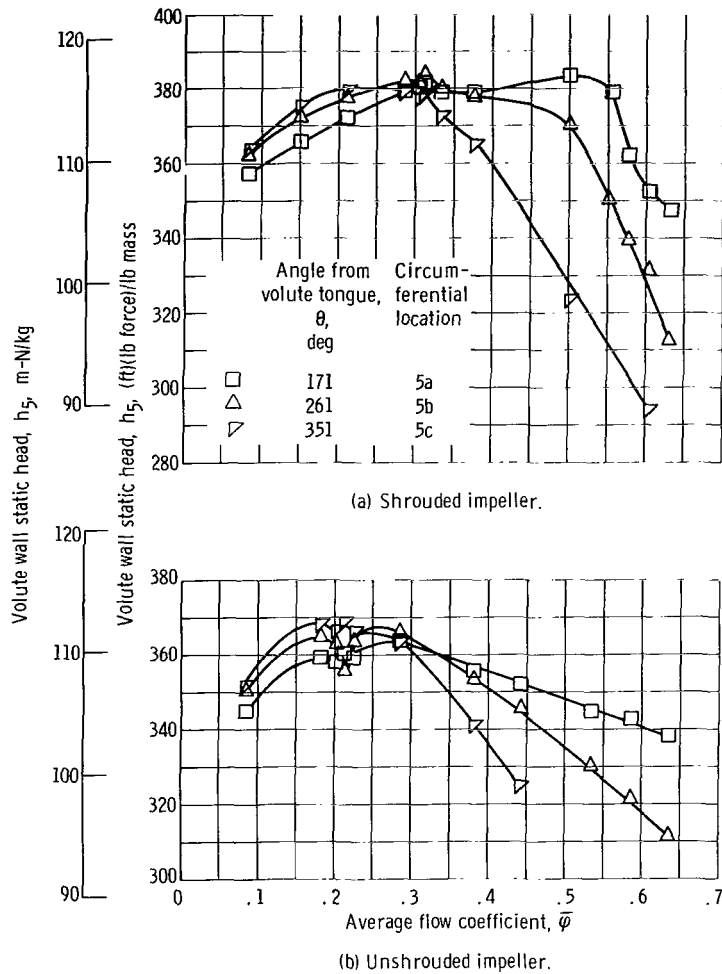
Figure 14. - Wall static head at three circumferential locations at volute measuring station (station 5). Net positive suction head, 192 feet per pound force per pound mass (58.5 m-N/kg).

magnitude of the circumferential gradients was different because of different matching of the impeller and volute.

As $\bar{\varphi}$ was decreased from the $\bar{\varphi}$ reference range, circumferential gradients were noted in the measurements, as indicated in figures 11 to 14. However, the gradients generally were not as great as at the higher $\bar{\varphi}$. The static head in the volute h_5 (fig. 14) and that at the outlet measuring station h_4 (fig. 13), increase with circumferential location; that is, the highest back pressure occurred near the volute tongue ($\theta = 360°$). This back pressure gradient is the reverse of the gradient at a $\bar{\varphi}$ greater than the reference range. With this variation of back pressure, ψ_4 and β_4 would be expected to increase with circumferential position. If β_4 is considered a first approximation to work input, or ψ_{id}, then for both impellers the energy addition was the largest near the volute tongue where the back pressure was the highest.

24

However, the ψ_4 (fig. 11) gradients show circumferential trends that are inconsistent with those of β_4, h_4, and h_5. One source of the apparent inconsistency is probably the impeller secondary flow loss. In general, as $\overline{\varphi}$ is decreased, blade passage velocity gradients increase, and secondary flows, flow separations, and tip-clearance flows increasingly affect the impeller flow conditions. Note that $\beta_4 > 90^O$ (fig. 12) was measured near the volute tongue. These results are interpreted as reverse flow or flow separation. Because of flow redistributions and losses associated with separated flow regions, the circumferential trends of ψ_4 and β_4 were not as consistent in this low $\overline{\varphi}$ range as at the higher $\overline{\varphi}$. However, the lowest ψ_4 (fig. 11) does consistently occur just downstream of the volute tongue ($\theta = 81^O$) where h_4 (fig. 13) is minimum.

In the $\overline{\varphi}$ range of 0.20 to 0.25, ψ_4 (figs. 11(b), (d), and (e)) and β_4 (figs. 12(d) to (f)) for the unshrouded impeller show sharp changes with $\overline{\varphi}$. Somewhat similar, but much smaller changes in ψ_4 (fig. 11) were noted for the shrouded impeller. Operation across these regions was repeated several times. The same dips were measured each time, which indicates that a more violent adjustment to the separation can be expected if the tip clearance is large.

The measurements from both impellers indicate that large circumferential variations of performance should be expected when an impeller with a single-discharge volute is operated over a wide flow range. Also, secondary flows can exert a strong influence on flow conditions at a low $\overline{\varphi}$.

Spanwise distributions of outlet parameters. - The circumferentially averaged head-rise coefficient $\hat{\psi}$, the flow coefficient $\hat{\varphi}$, and the flow angle $\hat{\beta}$ are presented for stations 3 (trailing edge) and 4 (outlet measuring station). Three additional parameters, the deviation angle $\hat{\delta}$, the slip factor $\hat{\mu}$, and the ideal head-rise coefficient $\hat{\psi}_{id}$, are presented at station 3. The data presented for station 4 (fig. 15) allow velocity diagrams to be computed from measured data. The spanwise variations of parameters at stations 3 and 4 are similar to changes in magnitude that reflect the change in radius and flow area. Consequently, the discussion is limited to the parameters computed for station 3 (fig. 16). The head-rise coefficient $\hat{\psi}_4$ is assumed to be the same at both stations 3 and 4.

Spanwise distributions of parameters at two $\overline{\varphi}$ which bracket the $\overline{\varphi}$ reference range are presented in figure 16 for each impeller. (A $\overline{\varphi}$ reference range, centered about $\overline{\varphi} \simeq 0.32$, was previously described in the section Outlet measurements.) Data are presented at $\overline{\varphi} = 0.286$ and 0.377 for the shrouded impeller and at $\overline{\varphi} = 0.285$ and 0.381 for the unshrouded impeller to illustrate flow conditions over the $\overline{\varphi}$ reference range.

For the shrouded impeller, all the parameters in figure 16(a) are essentially constant across the span at $\overline{\varphi} = 0.286$ and 0.377, which indicates that a shrouded radial-bladed impeller (or unshrouded impeller with a small ratio of tip clearance to blade span) could reasonably be designed or analyzed at $\overline{\varphi}_D$ with the use of only the midspan outlet parameters to represent spanwise average values.
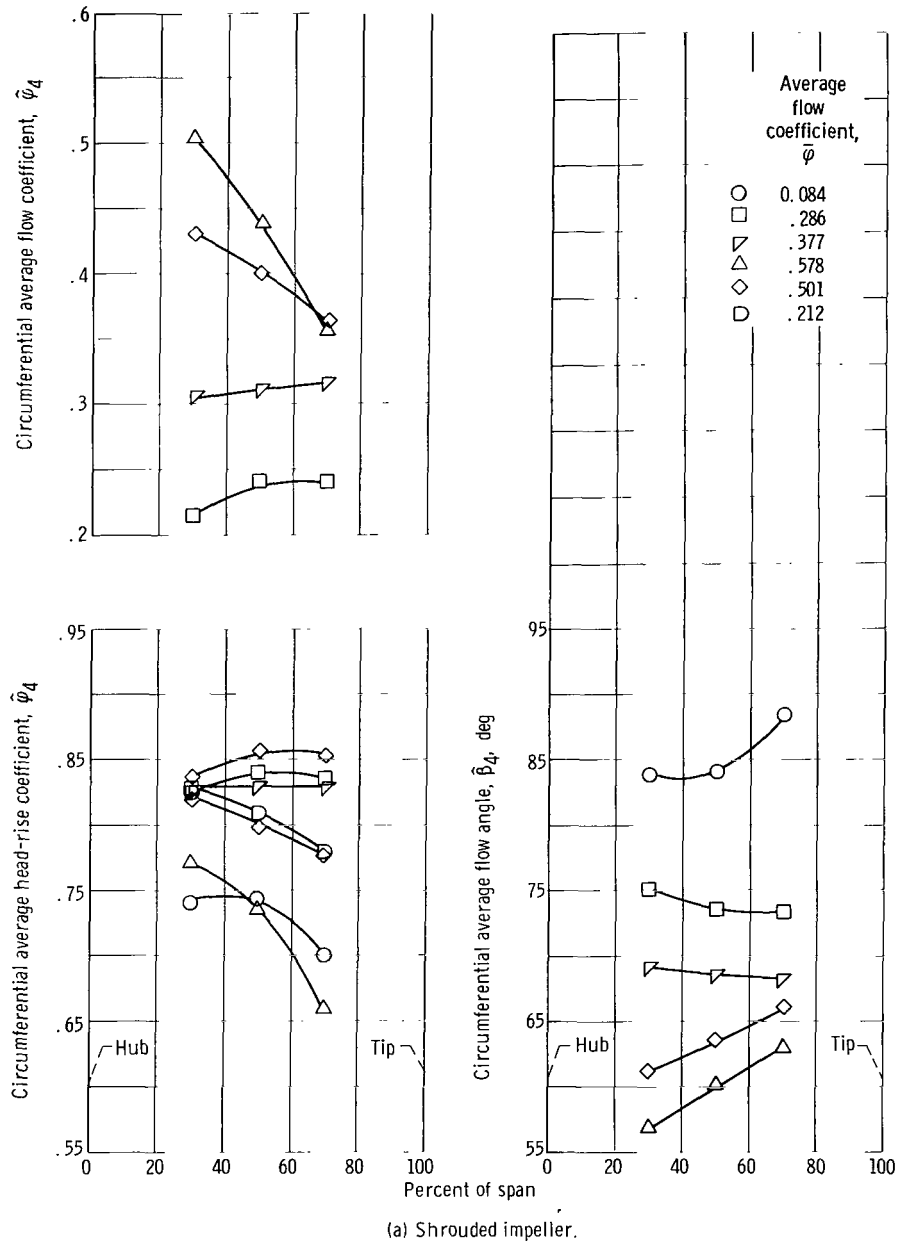
Figure 15. – Spanwise distribution of circumferential average performance and velocity-diagram parameters at outlet measuring station 4. Net positive suction head, 192 feet per pound force per pound mass (58.5 m-N/kg).

26
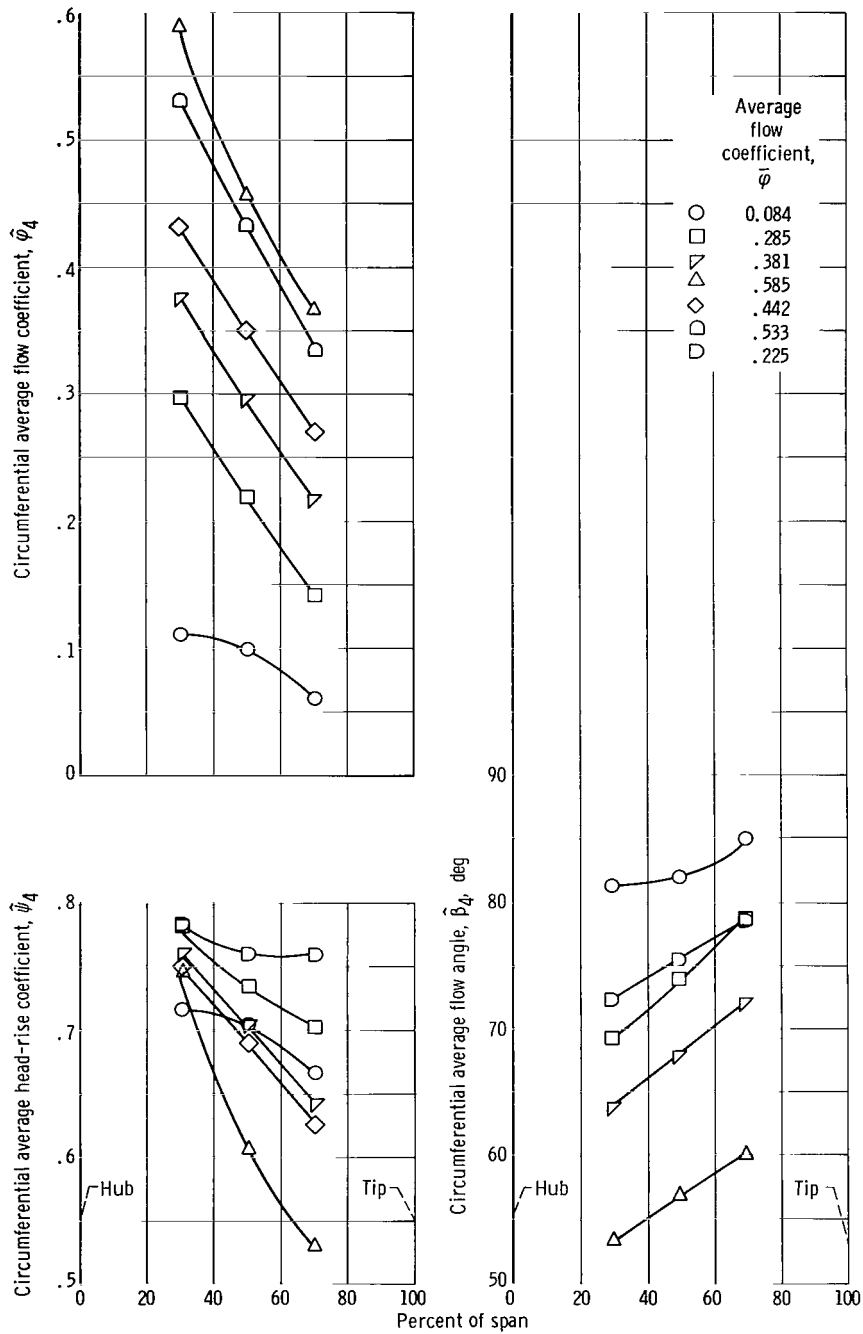
(b) Unshrouded impeller.

Figure 15. – Concluded.
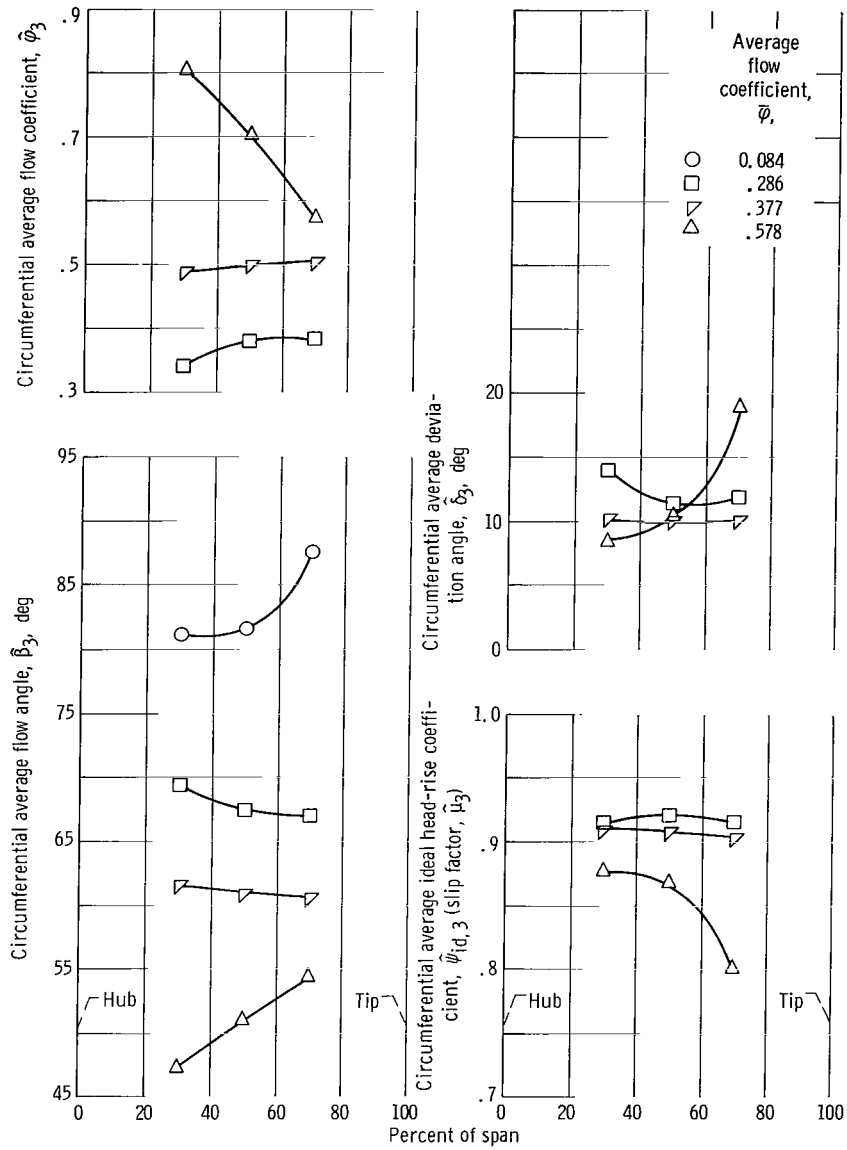
(a) Shrouded impeller.

Figure 16. - Spanwise distribution of circumferential average velocity-diagram parameters at blade trailing edge (station 3). Net positive suction head, 192 feet per pound force per pound mass (58.5 m-N/kg).
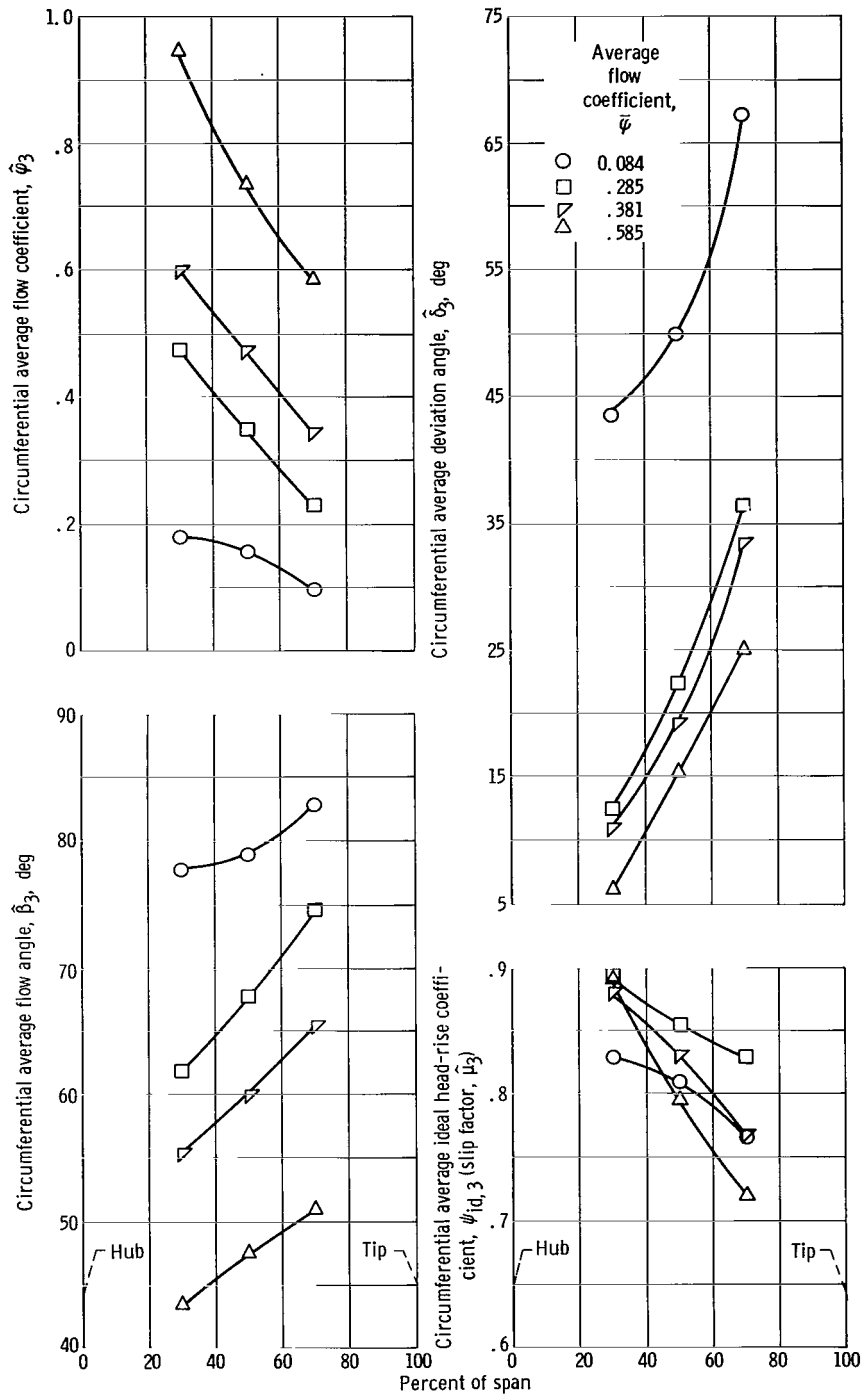
(b) Unshrouded impeller.

Figure 16. - Concluded.

29

In contrast, for the unshrouded impeller, significant spanwise gradients of all parameters (fig. 16(b)) are noted at $\overline{\varphi}$ = 0.285 and 0.381. The highest performance levels were measured in the hub region, with decreasing levels measured toward the tip. The spanwise variation of outlet parameters is probably the result of tip-clearance flow disturbances and losses. The work input of the blades, as indicated by $\hat{\psi}_{id,3}$ (fig. 16(b)), decreased from hub to tip. The head-rise coefficient $\hat{\psi}_4$ (fig. 15(b)) decreased slightly more along the span than did $\hat{\psi}_{id,3}$ (fig. 16(b)), which indicates that losses increased toward the tip. The major portion of the spanwise gradient of $\hat{\psi}_4$, however, resulted from the decrease of work input and not from increased losses. Note, also, that even near the hub, $\hat{\psi}_4$ (fig. 15(b)) for the unshrouded impeller is less than $\hat{\psi}_4$ (fig. 15(a)) for the shrouded impeller. This difference indicates that the redistributions of streamlines caused by tip-clearance flows affects the performance of all spanwise positions.

As $\overline{\varphi}$ was increased from the reference range, visual observations (ref. 2) indicated that cavitation in the tip region began at a $\overline{\varphi}$ of approximately 0.5. Moreover, the intensity of the cavitation increased with $\overline{\varphi}$ and was not symmetrical around the periphery of the impeller. Close examination of additional data taken on this rotor, but not presented in the report, indicated that, as $\overline{\varphi}$ was increased from the reference range, the spanwise gradients of flow parameters did not change unless affected by cavitation; this seems logical, since as $\overline{\varphi}$ is increased, the streamwise and blade-to-blade passage velocity (or pressure) gradients tend to decrease. This decrease, in turn, would tend to lessen the secondary flows that primarily affect spanwise gradients of flow conditions at the outlet of a centrifugal impeller.

At the high $\overline{\varphi}$ points presented ($\overline{\varphi}$ = 0.578 for the shrouded impeller and 0.585 for the unshrouded impeller), cavitation affects the spanwise distributions. Cavitation resulted in a performance deterioration in the tip region for both impellers (fig. 16). If cavitation were absent, the parametric values at 30 percent of the span from the hub would probably be unchanged. These values fix a basepoint for the spanwise distribution of the parameters whose spanwise gradients probably would be the same as those in the $\overline{\varphi}$ reference range. However, in an application of similar impellers with an inducer added, some cavitation at a high $\overline{\varphi}$ may be difficult to avoid. The full H_{sv} of 192 feet per pound force per pound mass (58.5 N-m/kg) used at a rotational speed of 3000 rpm represents an inducer head-rise coefficient of 0.652. This coefficient is two to three times larger than that achieved with usual inducer rotors. Thus, the trends shown at $\overline{\varphi}$ = 0.578 and 0.585 in figure 15 may not be unusual for most applications.

Data are shown in figures 15 and 16 for both impellers (at $\overline{\varphi}$ = 0.084) as $\overline{\varphi}$ is reduced from the reference range. Velocity-diagram parameters for the shrouded impeller could not be calculated because of transducer limitations. The spanwise gradients of parameters at $\overline{\varphi}$ = 0.084 differ from those in the reference range. The difference is probably caused by impeller secondary flows that tend to become stronger as φ is de-
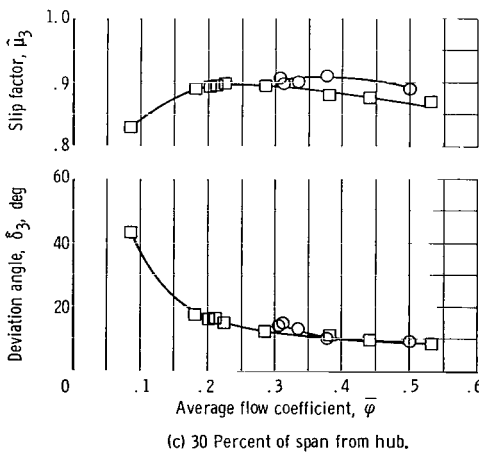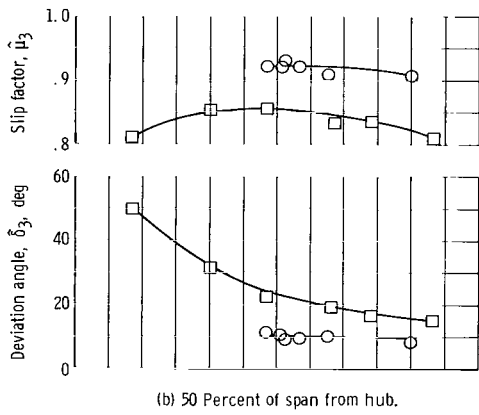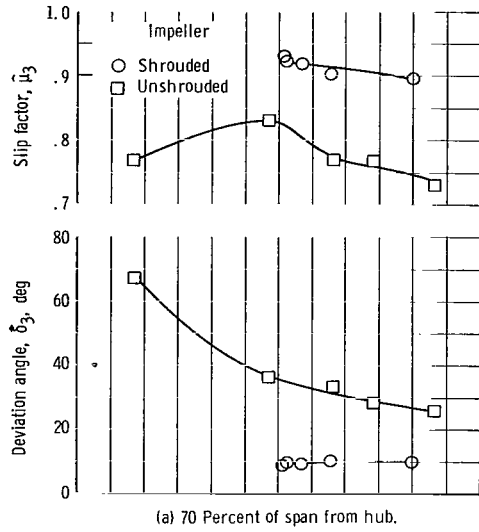
Figure 17. – Slip factor and deviation angle as function of flow coefficient for three span positions. Net positive suction head, 192 feet per pound force per pound mass (58.5 m-N/kg).

creased. Both the shrouded and unshrouded impellers show a performance dropoff in the blade tip regions.

Slip factor and deviation angle. - The flow leaving an impeller deviates from the blade direction. This deviation can be accounted for with the use of either the slip factor or the deviation angle. Normally, the slip factor is used because most design information is available in this form.

The slip factor must be predicted to estimate both the design and the off-design performance. Known parameters that influence the slip factor include the outlet blade angle, the number of blades, the blade height, and the flow coefficient. For a radial-bladed impeller, most prediction methods, such as those of Stodola and Busemann (ref. 5), give slip factor as a function of the number of blades and other impeller geometry. More recently, slip factors that varied with the flow rate were published by Stahler (ref. 6), who also proposed an empirical method in which the slip factor was presented as a linear function of the flow rate as well as a function of the impeller geometry. His data indicated that the deviation angle remained constant as the flow rate was changed.

Much experimental data will be required to evaluate and expand off-design prediction methods such as that proposed by Stahler (ref. 6). In this section, the variations of $\hat{\mu}_3$ and $\hat{\delta}_3$ with $\bar{\varphi}$ for the two impellers investigated are presented in figure 17, as a contribution to this area. Data are presented for three locations along the span. Values for $\bar{\varphi} > 0.55$ are not presented because of the possible effects of cavitation on the accuracy data. Values below $\bar{\varphi} = 0.3$ for the shrouded impeller were not available because of instrumentation limitations.

For the shrouded impeller at 50 percent of the span, $\hat{\mu}_3$ (fig. 17(b)) changes only slightly with $\bar{\varphi}$ and could be considered constant within a tolerance of ± 0.015. Over the flow range shown (82 to 135 percent of $\bar{\varphi}_D$), $\hat{\delta}_3$ (fig. 17(b)) is also constant with $\bar{\varphi}$.

At 30 percent of the span, $\hat{\mu}_3$ (fig. 17(c)) for the shrouded impeller can also be considered constant within ± 0.01. In the limited range from $\bar{\varphi} = 0.5$ to 0.3, $\hat{\delta}_3$ increased 6°. At 70 percent of the span (fig. 17(a)), $\hat{\mu}_3$ for the shrouded impeller increased gradually as $\bar{\varphi}$ was decreased; however, $\hat{\delta}_3$ was constant with $\bar{\varphi}$.

For the unshrouded impeller (figs. 17(a) to (c)), $\hat{\mu}_3$ and $\hat{\delta}_3$ vary with $\bar{\varphi}$ at all span positions except near the hub from $\bar{\varphi} = 0.30$ to 0.50. The largest variations of $\hat{\mu}_3$ and $\hat{\delta}_3$ occur near the tip (fig. 17(a)) and the least near the hub (fig. 17(c)). In general, the rate of change in $\hat{\mu}_3$ and $\hat{\delta}_3$ increases below $\bar{\varphi} = 0.3$.

The slip factors given in figure 17 were computed from circumferential averaged measurements. However, if the variation in back pressure around the impeller at $\bar{\varphi} > \bar{\varphi}_D$ (fig. 14) is considered, it is reasonable to assume that the slip factor also varied significantly around the circumference at $\bar{\varphi} > \bar{\varphi}_D$.

The slip factor data from this investigation are too limited to state any general conclusions. However, it was noted that $\hat{\delta}_3$ was constant over the limited flow range shown

for the shrouded impeller, as Stahler (ref. 6) suggested. For the unshrouded impeller, $\hat{\delta}_3$ was neither constant over the flow range nor across the span. The results for the unshrouded impeller may be influenced by the fact that the span at the outlet is only 0.191 inch (0.485 cm) and that the tip clearance was 0.025 inch (0.064 cm).

Cavitating Performance

Performance under noncavitating conditions was of primary interest in this investigation since the impeller was not designed for good cavitation performance and no inducer was used. However, a limited amount of performance data measured under cavitating conditions is presented to indicate how much pressure rise an inducer must provide for this impeller.

Overall performance. - The mass-averaged head-rise coefficient $\overline{\psi}$ and the hydraulic efficiency $\overline{\eta}$ are presented in figure 18 for both impellers. Noncavitating curves are included for comparison. The efficiency curves are not complete because of transducer limitations.

Some of the data of figure 18 were cross-plotted as $\overline{\psi}/\psi_{nc}$ against H_{sv} and are presented in figure 19. The curves of figure 19 show that, for the tip clearance used, $\overline{\psi}$ dropped off at a lower H_{sv} for the unshrouded impeller than that for the shrouded impeller. The same result was noted by Wood, et al. (ref. 7). At φ_D, $\overline{\psi}$ (fig. 19) began to decrease at a suction specific speed of 3765 (H_{sv} = 50 (ft)(lb force)/lb mass or 15 m-N/kg) for the unshrouded impeller and 3460 (H_{sv} = 56 (ft)(lb force)/lb mass or 18 m-N/kg) for the shrouded impeller.

Detailed performance. - Spanwise distributions of ψ are presented in figures 20 to 25 to give some insight into the way cavitation affects the performance of centrifugal impellers. The distributions measured at stations 4A, 4B, and 4C are shown for three values of $\overline{\varphi}$.

For the shrouded impeller (figs. 20 to 22), the noncavitating ψ (H_{sv} = 192 (ft) (lb force)/lb mass or 58.5 m-N/kg) is approximately constant along the span except for $\psi_{C,4}$ at $\overline{\varphi}$ = 0.45 and 0.525. The curves of $\psi_{C,4}$ for H_{sv} = 192 feet per pound force per pound mass (58.5 m-N/kg) at $\overline{\varphi}$ = 0.450 and 0.525 (figs. 21(c) and 22(c)) decrease toward the shroud, which indicates that some cavitation was present at θ = 351° (near volute tongue) for $\overline{\varphi} > 0.45$ and H_{sv} = 192 feet per pound force per pound mass (58.8 m-N/kg). Visual studies (ref. 2) verified the presence of cavitation in the sector of the unshrouded impeller near the volute tongue at these conditions. At a lower H_{sv}, cavitation caused ψ to decrease at all span locations, but the decrease was usually greatest near the shroud.
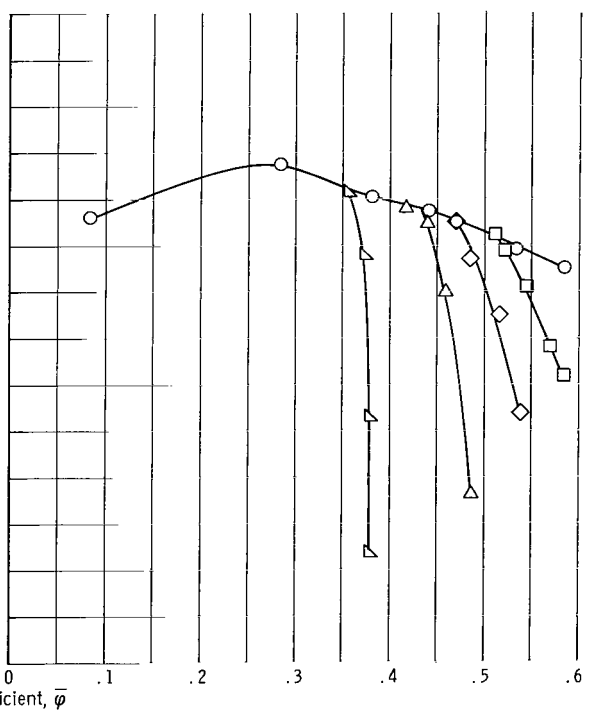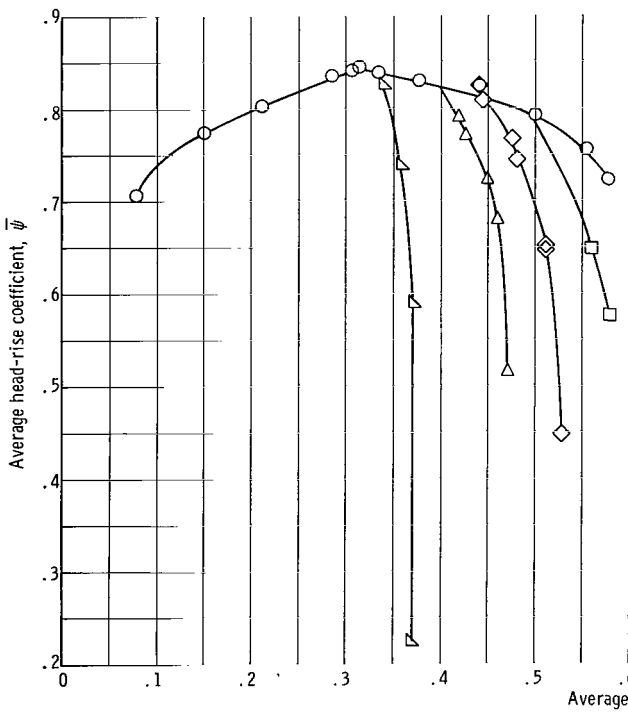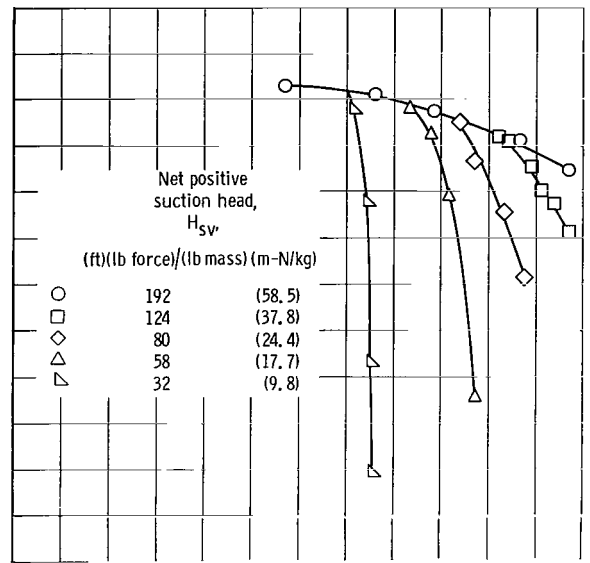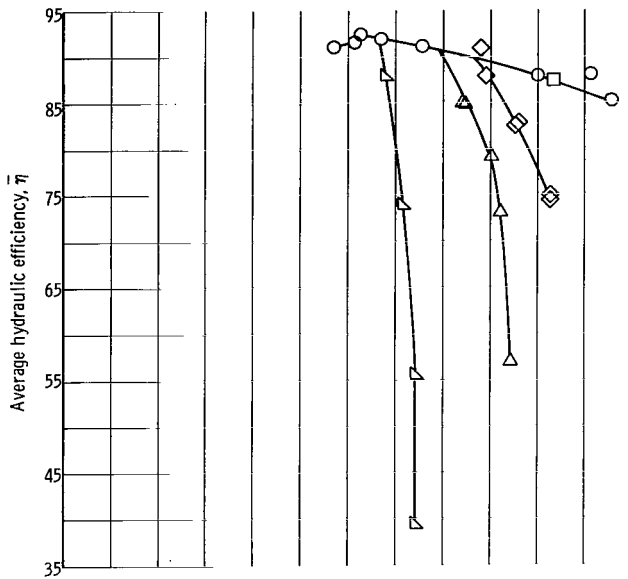
Figure 18. – Overall performance for cavitating conditions. Impeller outlet tip speed, 97.34 feet per second (29.67 m/sec).

Net positive
suction head,
H_{sv},

	(ft)(lb force)/(lb mass)	(m-N/kg)
○	192	(58.5)
□	124	(37.8)
◇	80	(24.4)
△	58	(17.7)
◁	32	(9.8)

(a) Shrouded impeller.

(b) Unshrouded impeller.
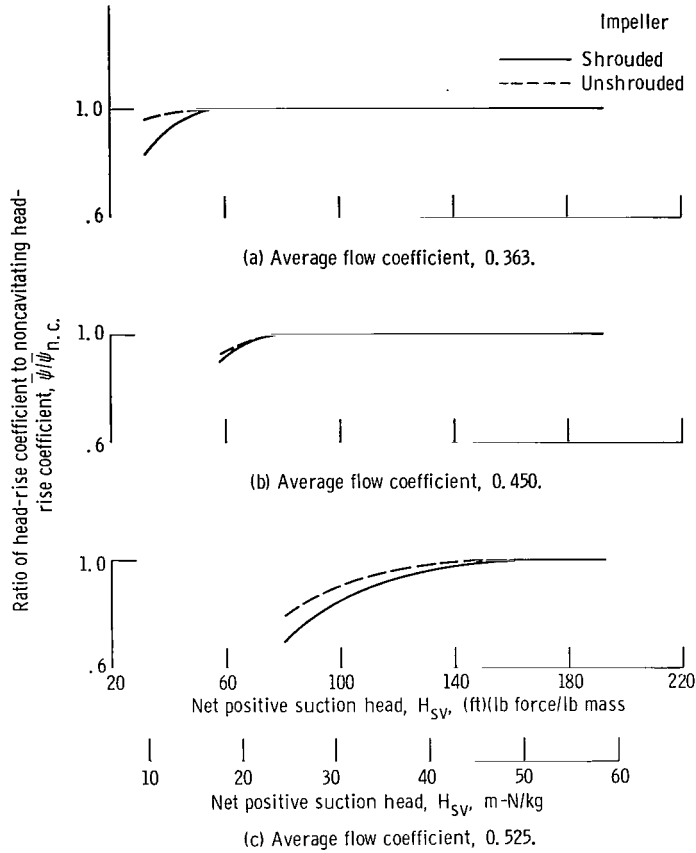
Figure 19. - Comparison of overall cavitating performance of shrouded and unshrouded impellers. Impeller outlet tip speed, 97.34 feet per second (29.67 m/sec).

The head-rise coefficients for the unshrouded impeller are shown in figures 23 to 25. The noncavitating ψ for the unshrouded impeller decreased along the span. The decrease in ψ caused by cavitation was approximately uniform along the span at all three $\overline{\varphi}$. For the flow range covered $(\overline{\varphi} > \overline{\varphi}_D)$, the greatest effect of cavitation on both impellers was noted in $\psi_{C,4}$ $(\theta = 351^O)$, and the smallest effect in $\psi_{B,4}$ $(\theta = 171^O)$. Visual studies of the unshrouded impeller (ref. 2) showed that the visible vapor was a maximum in the area of the tongue $(\theta = 360^O)$ and decreased progressively to $\theta \simeq 180^O$. This circumferential gradient of cavitation indicates that the sector of the impeller near the tongue was operating at a higher local flow rate than the rest of the impeller. A nonuniform flow rate is also indicated by circumferential gradients of ψ (fig. 11) and h_5 (fig. 14) under noncavitating conditions.

(a) Angle from volute tongue, 81°.

(b) Angle from volute tongue, 171°.

(c) Angle from volute tongue, 351°.
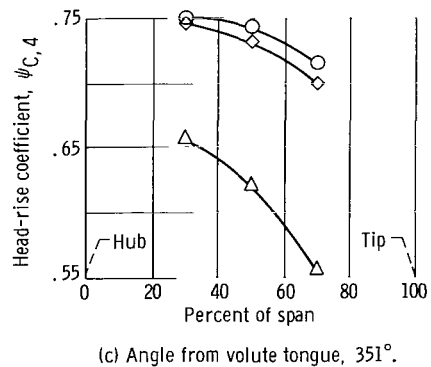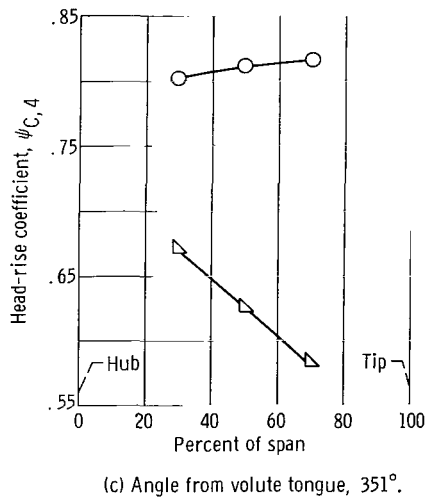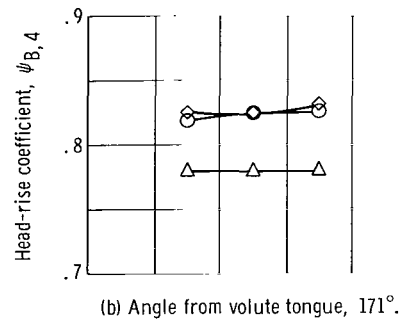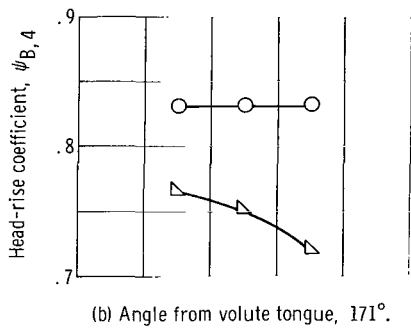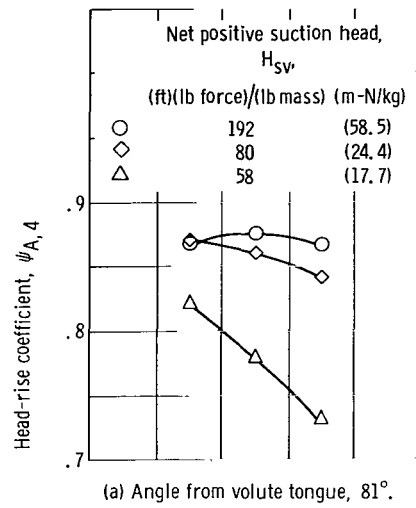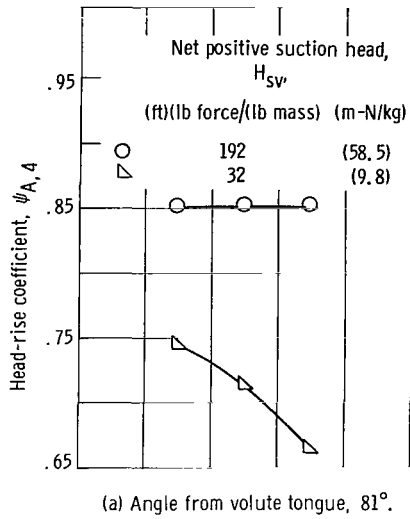
Figure 20. – Spanwise distributions of local head-rise coefficient for shrouded impeller under noncavitating and cavitating conditions at average flow coefficient of 0.366. Impeller outlet tip speed, 97.34 feet per second (29.67 m/sec).

(a) Angle from volute tongue, 81°.

(b) Angle from volute tongue, 171°.

(c) Angle from volute tongue, 351°.

Figure 21. – Spanwise distributions of local head-rise coefficient for shrouded impeller under noncavitating and cavitating conditions at average flow coefficient of 0.450. Impeller outlet tip speed, 97.34 feet per second (29.67 m/sec).
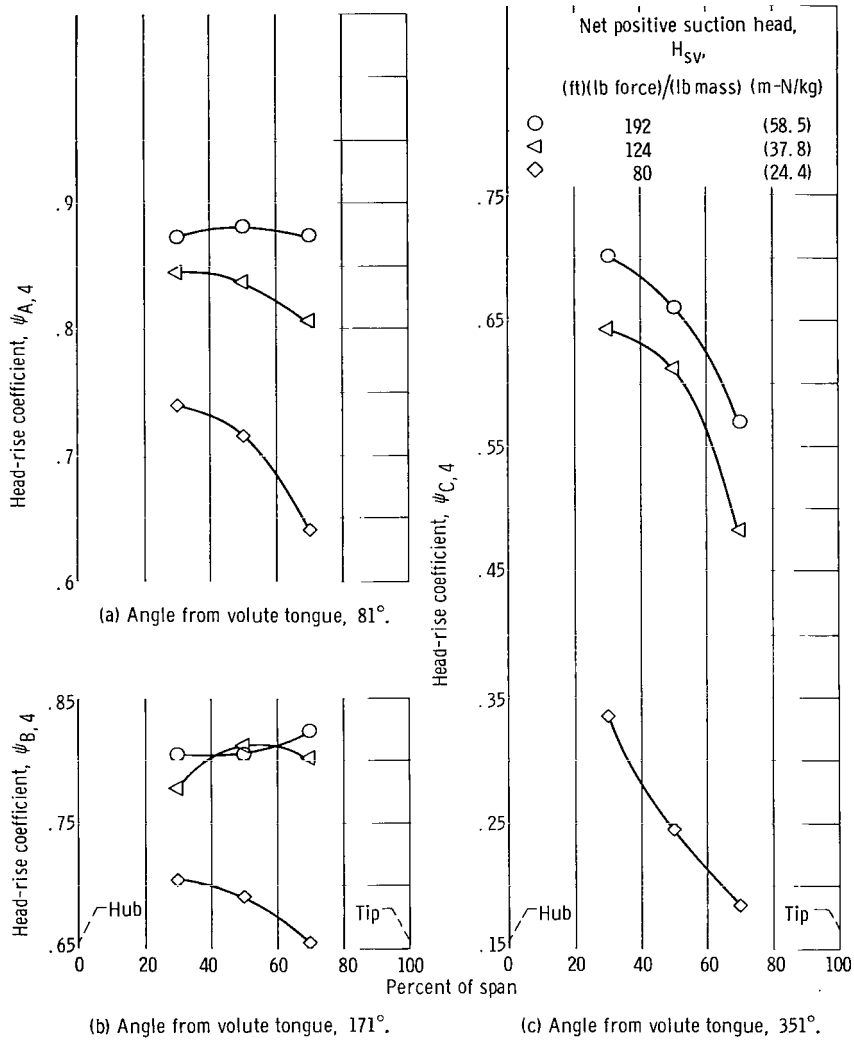
Figure 22. - Spanwise distributions of local head-rise coefficient for shrouded impeller under noncavitating and cavitating conditions at average flow coefficient of 0. 525. Impeller outlet tip speed, 97. 34 feet per second (29. 67 m/sec).

37

Net positive
suction head,
H_{sv}

	$\dfrac{\text{(ft)(lb force)}}{\text{lb mass}}$	$\left(\dfrac{\text{m-N}}{\text{kg}}\right)$
O	192	(58. 5)
△	32	(9. 8)
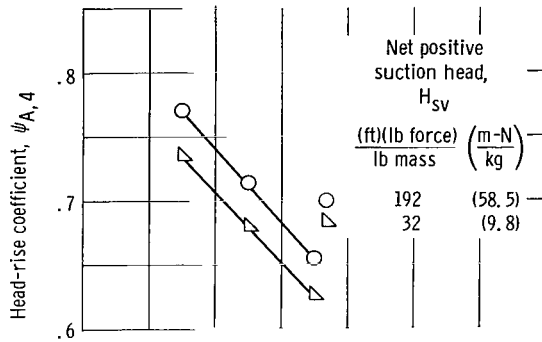
(a) Angle from volute tongue, 81°.
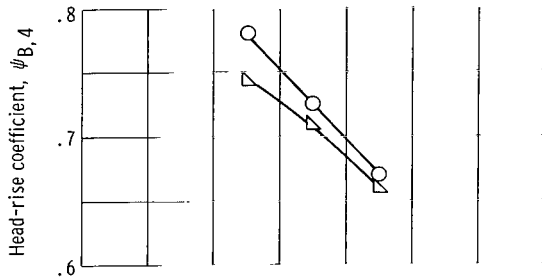
(b) Angle from volute tongue, 171°.
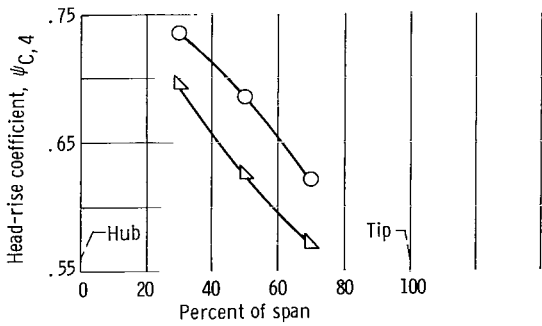
(c) Angle from volute tongue, 351°.

Figure 23. - Spanwise distributions of local head-rise coefficient for unshrouded impeller under cavitating and noncavitating conditions at average flow coefficient of 0.366. Impeller outlet tip speed, 97.34 feet per second (29.67 m/sec).

Net positive
suction head,
H_{sv}

	$\dfrac{\text{(ft)(lb force)}}{\text{lb mass}}$	$\left(\dfrac{\text{m-N}}{\text{kg}}\right)$
O	192	(58. 5)
△	58	(17. 7)
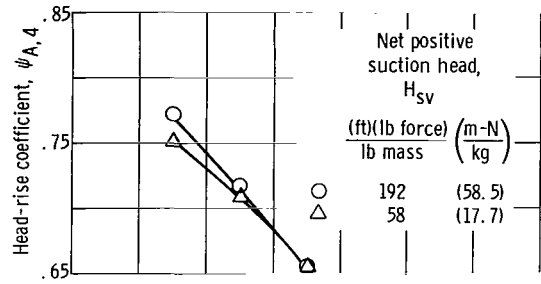
(a) Angle from volute tongue, 81°.
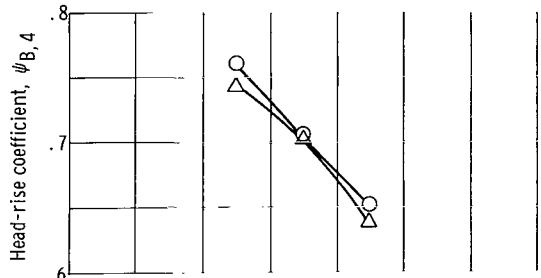
(b) Angle from volute tongue, 171°.
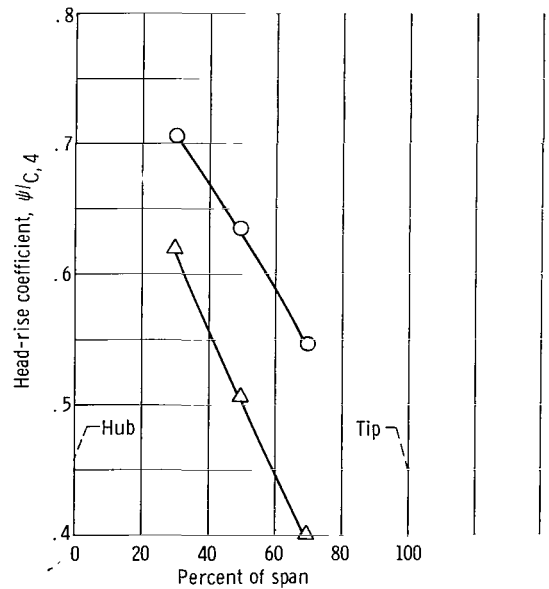
(c) Angle from volute tongue, 351°.

Figure 24. - Spanwise distributions of local head-rise coefficient for unshrouded impeller under cavitating and noncavitating conditions at average flow coefficient of 0.450. Impeller outlet tip speed, 97.34 feet per second (29.67 m/sec).

(a) Angle from volute tongue, 81°.

(b) Angle from volute tongue, 171°.

Net positive
suction head,
H_{sv}

$\dfrac{\text{(ft)(lb force)}}{\text{lb mass}}$	$\left(\dfrac{\text{m-N}}{\text{kg}}\right)$
○ 192	(58.5)
□ 124	(37.8)
◇ 80	(24.4)

Head-rise coefficient, $\psi_{A,4}$

Head-rise coefficient, $\psi_{B,4}$

Head-rise coefficient, $\psi_{C,4}$

Hub

Tip

Percent of span
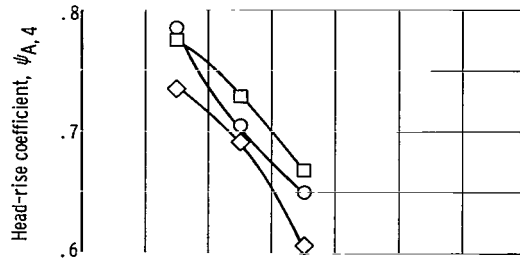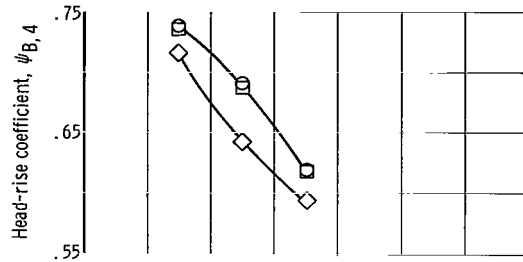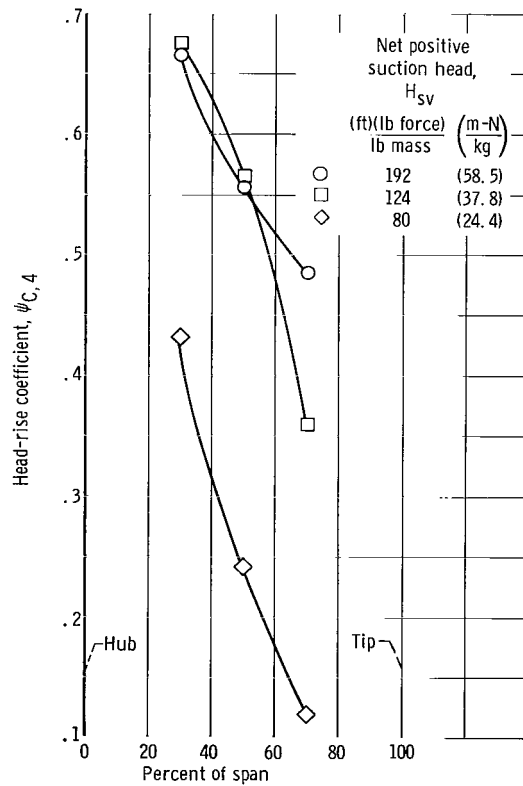
(c) Angle from volute tongue, 351°.

Figure 25. – Spanwise distributions of local head-rise
coefficient for unshrouded impeller under cavitating
and noncavitating conditions at average flow coef-
ficient of 0.525. Impeller outlet tip speed 97.34 feet
per second (29.67 m/sec).

39

APPLICATION OF RESULTS TO ANALYTICAL PROCEDURES

Various analytical procedures are utilized to predict both design and off-design flow conditions and performance of centrifugal pumps. An example of such a procedure is reported in reference 1. In general, the computed flow conditions from these procedures are somewhat idealized because flow conditions such as steady flow, circumferential periodicity of flow (same in all flow passages), and inviscid fluid flow must be assumed to obtain a solution. In this section, some observed real flow conditions are related to the idealized flow conditions of analytical procedures.

For the pump (i.e., impeller, vaneless diffuser, and single-discharge scroll) under study, the measurements indicated that flow conditions around the periphery of the impeller were the same at just one reference flow. As operation was varied to flows higher or lower than the reference flow, significant circumferential variations of flow conditions (figs. 11(a), (c), (e); 12 (a) to (c); 13(a); and 15(a)) were observed. The condition of identical flow in each blade passage was only realized at the reference flow.

In contrast, the analytical procedures compute the flow through one blade passage and assume that flow is the same in all other passages (circumferential periodicity of flow). This assumption evidently becomes less realistic as the operating point is moved away from the reference flow. The solutions obtained for flows other than the reference flow probably approximate an average of the varying flow conditions around the impeller. Therefore, in any analysis or comparative procedure, an awareness of this real flow condition may aid in evaluating conclusions.

The testing of both shrouded and unshrouded versions of the impeller permitted some indication of tip-clearance flow effects. For this relatively small impeller, the 0.025-inch (6.34-mm) tip clearance results in a tip-clearance to blade-span ratio of 13 percent at the impeller outlet (unshrouded). As discussed in the previous section, measurements showed significant differences in both the magnitudes and the spanwise distributions of outlet parameters for the two configurations. For example, $\hat{\psi}_4$ (figs. 15(a) and (b)) and $\hat{\mu}_3$ (figs. 16(a) and (b)) show the effects of tip-clearance flow. Tip-clearance flows would be expected to increase losses locally. The significant local effect on $\hat{\mu}_3$ indicates that energy addition was also reduced. Analytical procedures usually do not account for secondary flow effects, including tip-clearance flows. Thus, the analytical procedures are most applicable to shrouded impellers and to unshrouded impellers with low ratios of tip clearance to blade span.

In the exit region of the blade passages, the flow streamlines deviate significantly from the direction of the blades. One method of accounting for this deviation is to apply a slip factor. In the procedure of reference 1, for example, the slip factor is an input. Its value may be obtained from tests from a similar type rotor or from a correlation such as the Busemann correction for slip, presented in reference 5. For the impeller inves-

tigated herein, a slip factor of 0.9 is obtained from the Busemann theory. Measured values from the shrouded impeller indicated slip factors ranging from 0.89 to 0.93 for the $\bar{\varphi}$ range of 0.3 to 0.5. Over this $\bar{\varphi}$ range, $\hat{\mu}_3$ (fig. 12) did not vary significantly either across the span or with $\bar{\varphi}$. Thus, the Busemann correction for slip was reasonably accurate for the shrouded impeller. However, results from the unshrouded impeller indicated that $\hat{\mu}_3$ (fig. 17) varied along the span with $\bar{\varphi}$. Values ranged from about 0.9 near the hub to values as low as 0.7 near the tip. These results indicate that, for impellers with high ratios of tip clearance to blade span, an adjustment to the Busemann correction for slip is necessary. The adjustment should result in an average slip factor less than the value of the Busemann correction for slip.

At a $\bar{\varphi}$ below 0.18, measurements at the inlet measuring station indicated reverse flows in the blade tip region. Indications of the reverse flow region were $\beta_1 > 90°$ (figs. 8(a) and 9) and local H_1 values (figs. 8(a) and (b)) that exceeded the upstream average H_1. These measurements were interpreted to indicate that energized fluid in the blade passage was flowing back into the inlet pipe.

For comparison, the analytical procedure of reference 1, modified to calculate the size of theoretical eddy regions, was used to calculate the idealized flow field at $\bar{\varphi} = 0.17$. In this procedure, the calculation of zero or negative through-flow velocities is assumed to be evidence of an eddy, or reverse flow, region. At $\bar{\varphi} = 0.17$, an eddy region was

— (a) Tip.

—(b) Hub.
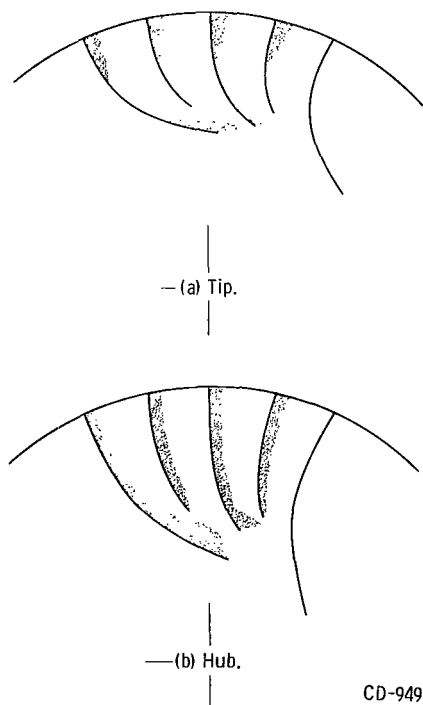
CD-9491

Figure 26. - Location and extent of eddy regions calculated by analytical procedure at average flow coefficient of 0.17.

41

calculated to be near the main blade pressure surface and extended along the entire blade span near the leading edge. The sketches of figure 26 show the extent of the eddy regions calculated on the hub and tip stream surfaces. The eddy region was largest near the hub where it extended across one-fourth of the passage between the main blades near the leading edge. However, the measurements from this investigation were not sufficient to establish a conclusive relation between the measured and the calculated eddy regions.

CONCLUDING REMARKS

A shrouded and an unshrouded version of a 7.44-inch- (18.89-cm-) diameter centrifugal pump were tested in room-temperature water. The impeller was designed with splitter blades to control passage pressure gradients. The pump was operated from 173 percent of the design flow coefficient to shut off with no unusual facility vibration or noise. The investigation provided detailed test measurements that contribute to a better understanding of real flows in radial-bladed centrifugal pumps and to a better prediction of performance. Both overall and detailed impeller performance were presented for noncavitating conditions. Where possible, applications of the test results to analytical procedures were made. Also, some cavitation performance and circumferential static-pressure gradients around the volute were presented.

For the pump configuration tested (impeller and single-discharge volute), axisymmetric flow conditions in the impeller discharge were obtained over only a narrow reference flow range. At other flows, circumferential gradients of volute back pressure caused varying degrees of asymmetry in the impeller-discharge flow conditions. The asymmetries were essentially the same for both impellers. At flows higher than the reference flow, the back pressure and head rise were the lowest near the volute tongue of the impeller; under cavitating conditions, the greatest effect of cavitation on local head rise occurred in this same area. For flows below the reference flow, the back pressure was the highest near the volute tongue. The circumferential gradients of impeller-discharge flow conditions were smaller than those obtained at the higher flows. Asymmetry of performance should be considered in locating test instrumentation to measure pump performance. The large asymmetries of discharge flow conditions must also be considered in the interpretation of analytical procedure solutions.

Results from the shrouded and unshrouded versions of the impeller indicate trends in flow conditions that may be expected as the ratio of tip clearance to blade span is varied from 0 to 13 percent. Near the design flow coefficient, the distributions of circumferential average outlet parameters were approximately constant across the span of the shrouded impeller. However, for the unshrouded impeller, the outlet parameters varied substantially across the span, and the performance was lower than that of the shrouded

impeller at all spanwise locations, with the greatest differences being near the tip. The design and analysis of an impeller with a low ratio of tip clearance to outlet blade span, with the use of only spanwise average outlet parameters, is reasonable.

For the shrouded impeller, slip factors and deviation angles not only were approximately constant across the span, but also were approximately constant over most of the span as the flow coefficient was varied from 82 to 135 percent of the design flow coefficient. The slip factor over this flow range compared closely with the Busemann correction for slip. For the unshrouded impeller, the slip factors and deviation angles changed with the flow coefficient over most of the blade span. The measured slip factors for the unshrouded impeller indicate that downward adjustments to the Busemann correction for slip are necessary when the ratio of tip clearance to blade span is large.

The effects of tip-clearance flows on the outlet parameters were reflected in the overall performance. Both the average head-rise coefficient and the hydraulic efficiency were higher for the shrouded impeller than those for the unshrouded impeller under noncavitating conditions.

At flow coefficients lower than design, two real flow phenomena were indicated by the detailed measurements. At the inlet, a reverse flow near the outer casing was detected at flow coefficients below 0.18 for both impellers. A potential flow solution at this flow coefficient also indicated an eddy region on the blade pressure surface near the leading edge. Measurements from this investigation were insufficient to associate the measured and calculated eddy regions conclusively.

A dip or dropoff was noted in most of the local head-rise coefficients at an average flow coefficient of 0.31 for the shrouded impeller and 0.21 for the unshrouded impeller. These abrupt changes in performance are thought to result from flow separation along the blade suction surface.

The cavitation performance of the unshrouded impeller appeared to be slightly better than that of the shrouded impeller. At the design flow coefficient, the unshrouded impeller head rise began to decrease at a suction specific speed of 3765. For the shrouded impeller, the head rise was decreased by cavitation at a suction specific speed of 3460.

Lewis Research Center,
National Aeronautics and Space Administration,
Cleveland, Ohio, January 30, 1968,
128-31-06-28-22.

APPENDIX A

SYMBOLS

A area, ft^2; m^2

e distance from casing to survey measurement location of station 1 (fig. 1), in.; cm

f distance from casing to survey measurement location at station 4 (fig. 1), in.; cm

g_c gravitational conversion factor, $32.17 \dfrac{(\text{lb mass})(\text{ft})}{(\text{lb force})(\text{sec}^2)}$

H total head, $\dfrac{(\text{ft})(\text{lb force})}{\text{lb mass}}$; $\dfrac{\text{m-N}}{\text{kg}}$

ΔH head rise (eqs. (B3), (B16), and (B18)), $\dfrac{(\text{ft})(\text{lb force})}{\text{lb mass}}$; $\dfrac{\text{m-N}}{\text{kg}}$

H_{sv} net positive suction head (eq. (B21)), $\dfrac{(\text{ft})(\text{lb force})}{\text{lb mass}}$; $\dfrac{\text{m-N}}{\text{kg}}$

h wall static head, $\dfrac{(\text{ft})(\text{lb force})}{\text{lb mass}}$; $\dfrac{\text{m-N}}{\text{kg}}$

h_v vapor head, $\dfrac{(\text{ft})(\text{lb force})}{\text{lb mass}}$; $\dfrac{\text{m-N}}{\text{kg}}$

i incidence angle (eq. (B2)), deg

N rotative speed, rpm

N_s specific speed (eq. (B22))

Q flow rate, gal/min; m^3/sec

Q_o orifice measured flow rate, gal/min; m^3/sec

r radius, in.; cm

s suction specific speed in units of rpm (eq. (B23)), gal/min, and $\dfrac{(\text{ft})(\text{lb force})}{\text{lb mass}}$

U rotor tangential velocity, ft/sec; m/sec

V fluid velocity, ft/sec; m/sec

z axial dimension, in.; cm

α volute angle, deg

β flow angle (angle between direction of flow and meridional plane), deg

γ angle from radius through suction surface at outlet tip of main blade (table I), rad

δ deviation angle (angle between outlet relative velocity and outlet blade angle), deg

η hydraulic efficiency (eq. (B20)), percent

θ angle from volute tongue (fig. 1), deg

κ blade angle (angle between tangent to blade mean camber line and meridional plane), deg

μ slip factor (eq. (B12))

φ flow coefficient (eqs. (B1), (B10), and (B15))

ψ head-rise coefficient (eqs. (B4), (B17), and (B19))

Subscripts:

A	location 81° from tongue in direction of flow
a	location 36° from tongue in direction of flow
B	location 171° from tongue in direction of flow
b	location 126° from tongue in direction of flow
C	location 351° from tongue in direction of flow
c	location 216° from tongue in direction of flow
D	design
d	location 306° from tongue in direction of flow
h	hub
id	ideal
j	iteration index on circumferential location A, B, or C
k	iteration index on instrumentation and/or calculation station 1, 2, 3, or 4
L	loss
m	meridional direction
n	iteration index on span positions 1 to 5
n.c.	noncavitating
o	orifice
t	tip
v	volute
z	axial direction
θ	tangential direction
1	inlet measuring station
2	blade leading edge
3	blade trailing edge
4	outlet measuring station
5	volute measuring station

Superscripts:

$'$	relative to impeller
$-$	circumferential and spanwise average quantity
$\hat{}$	circumferential average quantity

APPENDIX B

FLOW PARAMETER EQUATIONS

Local Parameter Equations

Inlet local flow coefficient:

$$\varphi_k = \frac{V_{m,k}}{U_{t,2}} \qquad k = 1, 2 \tag{B1}$$

Incidence angle:

$$i = \beta_2' - \kappa_2 \tag{B2}$$

Local head rise:

$$H_j = H_{j,4} - H_1 \qquad j = A, B, C \tag{B3}$$

Local head-rise coefficient:

$$\psi_j = \frac{g_c \Delta H_j}{U_{t,3}^2} \qquad j = A, B, C \tag{B4}$$

Circumferential Averaged Parameter Equations

Circumferential average total head:

$$\hat{H}_4 = \frac{1}{3}(H_{A,4} + H_{B,4} + H_{C,4}) \tag{B5}$$

Circumferential average wall static head:

$$\hat{h}_4 = \frac{1}{4}(h_{a,4} + h_{b,4} + h_{c,4} + h_{d,4}) \tag{B6}$$

Circumferential average velocity:

$$\hat{V}_4 = 2g_c(\hat{H}_4 - \hat{h}_4)^{1/2} \tag{B7}$$

Circumferential average flow angle:

$$\hat{\beta}_4 = \frac{1}{3}(\beta_{A,4} + \beta_{B,4} + \beta_{C,4}) \tag{B8}$$

Circumferential average meridional velocity:

$$\hat{V}_{m,4} = \hat{V}_4 \cos \hat{\beta}_4 \tag{B9}$$

Outlet flow coefficient:

$$\hat{\varphi}_k = \frac{\hat{V}_{m,k}}{U_{t,3}} \qquad k = 3, 4 \tag{B10}$$

Deviation angle:

$$\hat{\delta}_3 = \hat{\beta}_3' - \kappa_3 \tag{B11}$$

Slip factor:

$$\hat{\mu}_3 = \frac{V_{\theta,3}}{U_{t,3}} \tag{B12}$$

Ideal head rise:

$$\Delta H_{id} = \frac{1}{g_c}(U_3\hat{V}_{\theta,3} - U_2\hat{V}_{\theta,2})$$

in this investigation, $\hat{V}_{\theta,2}$ is considered to be 0 in all calculations and the equation becomes

$$\frac{1}{g_c}(U_3\hat{V}_{\theta,3}) \tag{B13}$$

Ideal head-rise coefficient:

$$\hat{\psi}_{id} = \frac{g_c\,\Delta H_{id}}{U_{t,3}^2} \tag{B14}$$

since

$$U_3 = U_{t,3}$$

$$\hat{\psi}_{id} = \frac{V_{\theta,3}}{U_{t,3}}$$

Overall Parameter Equations

Average flow coefficient:

$$\overline{\varphi} = \frac{V_z}{U_{t,2}} = \frac{Q_o(144)}{\left(r_{t,2}^2 - r_{h,2}^2\right) U_{t,1}\left(448.8\right)} \tag{B15}$$

Average head rise:

$$\Delta\overline{H} = \frac{1}{9}\sum_{j=A}^{C}\sum_{n=1}^{3}\Delta H_{j,n} \tag{B16}$$

Average head-rise coefficient:

$$\overline{\psi} = \frac{g_c\,\Delta\overline{H}}{U_{t,3}^2} \tag{B17}$$

48

Average ideal head rise:

$$\Delta \overline{H}_{id} = \frac{1}{g_c} (\overline{U}_3 \overline{V}_{\theta,3} - \overline{U}_2 \overline{V}_{\theta,2})$$

$$= \frac{1}{g_c} \left(\frac{\sum\limits_{n=1}^{3} U_{n,3} \hat{V}_{\theta,n,3}}{3} - \frac{\sum\limits_{n=2}^{4} U_{n,2} \hat{V}_{\theta,n,2}}{3} \right)$$

$$= \frac{1}{g_c} \frac{1}{3} \left(\sum\limits_{n=1}^{3} U_{n,3} \hat{V}_{\theta,n,3} \right) \quad \text{for } V_{\theta,2} = 0 \tag{B18}$$

Average ideal head-rise coefficient:

$$\overline{\psi}_{id} = \frac{g_c}{U_{t,3}^2} \Delta \overline{H}_{id} \tag{B19}$$

Average hydraulic efficiency:

$$\overline{\eta} = \frac{\overline{\psi}}{\overline{\psi}_{id}} 100 \tag{B20}$$

Net positive suction head:

$$H_{sv} = H_1 - h_v \tag{B21}$$

Specific speed:

$$N_s = \frac{N(Q_o)^{1/2}}{(\Delta H)^{3/4}} \tag{B22}$$

Suction specific speed:

$$S = \frac{N\left(Q_o\right)^{1/2}}{H_{sv}^{3/4}}$$ (B23)

Integrated inlet weight flow:

$$Q_1 = \sum_{n=1}^{5} V_{m,n,1} A_{n,1} (448.86)$$ (B24)

Integrated outlet weight flow:

$$Q_4 = \sum_{n=1}^{3} V_{m,n,4} A_{n,4} (448.86)$$ (B25)

50

APPENDIX C

CALCULATION OF FLOW CONDITIONS AT BLADE LEADING AND TRAILING EDGES

The inlet and outlet measuring stations (stations 1 and 4, fig. 1(b)) were located some distance from the leading and trailing edges of the impeller blades. Therefore, since the flow conditions at these blade edges must be known, the following procedures were used in this investigation to deduce the flow conditions at the leading and trailing edge stations from the measured flow conditions at the inlet and outlet measuring stations.

At the inlet, streamlines from the measurement locations at station 1 (fig. 1) were defined by assuming that the cross-sectional area of a streamtube is the same fraction of the total flow area at both the inlet measuring station (station 1) and at the blade leading edge (station 2). The streamlines adjacent to the hub and casing were assumed to be parallel to those surfaces. The slope and curvature of the streamlines were assumed to vary linearly from the hub to the casing.

The meridional velocity of each streamline was calculated at the leading edge with the use of the radial equilibrium equation and with the assumptions of a zero tangential velocity (but including streamline curvature) and a total head constant along a streamline from station 1 to station 2 (i.e., no loss). This meridional velocity distribution and the flow area at station 2 were used to calculate an overall flow rate, which, through an iterative process, converged to the orifice flow rate. Thus, an overall continuity was satisfied. To satisfy continuity on a stream tube basis involved another iteration to determine streamline locations. This iteration was considered too complicated for the available data reduction program.

Tangential velocity was essentially zero at the blade leading edge (station 2), so the calculated meridional velocity and the blade speed were used to calculate velocity-diagram parameters.

For the outlet, the procedure was simpler. Streamlines were again defined by assuming that the cross-sectional area of a streamtube at the trailing edge was the same fraction of the total flow area as it was at the outlet measuring station (station 4).

Conservation of angular momentum was used to determine the tangential velocity $V_{\theta,3}$, at the trailing edge. The radial velocity $V_{m,3}$ at the trailing edge was determined by requiring that continuity be satisfied in each streamtube from the trailing edge (station 3) to the outlet measuring station (station 4). With these two velocity components and the blade speed U_3, the velocity-diagram parameters at the trailing edge were calculated.

REFERENCES

1. Stockman, Norbert O.; and Kramer, John L.: Method for Design of Pump Impellers Using a High-Speed Digital Computer. NASA TN D-1562, 1963.

2. Soltis, Richard F.; and Miller, Max J.: Visual Observations of Flow Through a Radial-Bladed Centrifugal Impeller. NASA TN D-4282, 1968.

3. Stepanoff, Alexey J.: Centrifugal and Axial Flow Pumps. Second ed., John Wiley & Sons, Inc., 1957.

4. Crouse, James E.; Montgomery, John C.; and Soltis, Richard F.: Investigation of the Performance of an Axial-Flow-Pump Stage Designed by the Blade-Element Theory-Design and Overall Performance. NASA TN D-591, 1961.

5. Wislicenus, George F.: Fluid Mechanics of Turbomachinery. McGraw-Hill Book Co., Inc., 1947.

6. Stahler, Alfred F.: The Slip Factor of a Radial Bladed Centrifugal Compressor. J. Eng. Power, vol. 87, no. 2, Apr. 1965, pp. 181-192.

7. Wood, G. M.; Welna, H.; and Lamers, R. P.: Tip-Clearance Effects in Centrifugal Pumps. J. Basic Eng., vol. 87, no. 4, Dec. 1965, pp. 932-940.

"The aeronautical and space activities of the United States shall be conducted so as to contribute . . . to the expansion of human knowledge of phenomena in the atmosphere and space. The Administration shall provide for the widest practicable and appropriate dissemination of information concerning its activities and the results thereof."

— NATIONAL AERONAUTICS AND SPACE ACT OF 1958

NASA SCIENTIFIC AND TECHNICAL PUBLICATIONS

TECHNICAL REPORTS: Scientific and technical information considered important, complete, and a lasting contribution to existing knowledge.

TECHNICAL NOTES: Information less broad in scope but nevertheless of importance as a contribution to existing knowledge.

TECHNICAL MEMORANDUMS: Information receiving limited distribution because of preliminary data, security classification, or other reasons.

CONTRACTOR REPORTS: Scientific and technical information generated under a NASA contract or grant and considered an important contribution to existing knowledge.

TECHNICAL TRANSLATIONS: Information published in a foreign language considered to merit NASA distribution in English.

SPECIAL PUBLICATIONS: Information derived from or of value to NASA activities. Publications include conference proceedings, monographs, data compilations, handbooks, sourcebooks, and special bibliographies.

TECHNOLOGY UTILIZATION PUBLICATIONS: Information on technology used by NASA that may be of particular interest in commercial and other non-aerospace applications. Publications include Tech Briefs, Technology Utilization Reports and Notes, and Technology Surveys.

Details on the availability of these publications may be obtained from:

SCIENTIFIC AND TECHNICAL INFORMATION DIVISION

NATIONAL AERONAUTICS AND SPACE ADMINISTRATION
Washington, D.C. 20546